Supplementary Materials for

Reduced El Niño–Southern Oscillation during the Last Glacial Maximum

Heather L. Ford,* A. Christina Ravelo, Pratigya J. Polissar

*Corresponding author. E-mail: hford@ldeo.columbia.edu

Published 16 January 2015, *Science* **347**, 255 (2015)
DOI: 10.1126/science.1258437

This PDF file includes:

Other Supplementary Material for this manuscript includes the following:
(available at www.sciencemag.org/content/347/6219/255/suppl/DC1)

Database S1

Materials and Methods

Site Locations

We reconstructed surface and subsurface temperature variability at Ocean Drilling Program (ODP) Site 806 in the Western Equatorial Pacific (WEP) warm pool and ODP Site 849 in the Eastern Equatorial Pacific (EEP) cold tongue (Fig. S1). Compared to several previous reconstructions(*11-13*, *33*, *34*) our sites are better located to directly monitor changes in SST and thermocline depth strongly associated with ENSO dynamics. ODP Site 806, located on the Ontong Java Plateau (0°N, 159°E, 2520 m water depth) is used to monitor the mean state and variability in the Western Equatorial Pacific (WEP) Ocean. ODP Site 849, located within the core of the equatorial cold tongue extension (0°N, 110°W, 3839 m water depth) is used to monitor the mean state and variability in the Eastern Equatorial Pacific (EEP) Ocean. Equatorial Pacific ODP Sites 806 (WEP) and 849 (EEP) were selected because these sites experience large interannual and centennial variability in the modern ocean (Fig. S1). Age models for each site are based on high-resolution benthic isotope records(*35*, *36*). Using Analyseries(*37*) the previous age model for Site 849(*36*) was slightly adjusted to better match with the LR04 Last Glacial Maximum (LGM) and deglacial period. Ages for core-top samples were calculated using the average sedimentation rate for the last 100 kyrs (Table S1). Additionally, discrete sediment samples from these sites integrate several hundreds of years of variability. While secular SST trends over the timespan represented by a sample could influence reconstructed variability at these sites, the relatively small SST changes over <1000 years documented in these regions(*38*, *39*) suggests that seasonal and interannual frequencies of variation dominate the variability that our samples record.

Foraminifera Analysis

In order to investigate climate variability from the mid-Holocene to the Last Glacial Maximum and glacial period, surface and subsurface-dwelling individual foraminifera shells from Sites 806 and 849 were analyzed. Individual shells of surface-dwelling *Globigerinoides sacculifer* (without final sac-like chamber) and subsurface-dwelling *Globorotalia tumida* were picked for analysis (Table S3). Due to their preferred depth habitat, *G. sacculifer* were used to construct shallow mixed layer temperatures (~15 m), and *G. tumida* were used to construct subsurface temperatures [depth habitat ~100 m, independent of thermocline depth(*26*, *40*)]. Approximately 60-70 individuals of *G. sacculifer* and *G. tumida* were analyzed for minor elements and, in some instances, depth intervals were combined (Table S3). To minimize size dependent ontogenetic/kinetic effects on geochemical composition, only individuals from a restricted size range (355-425 μm) were analyzed. Individuals of *G. sacculfer* were analyzed via laser ablation on an Inductively Coupled Plasma-Mass Spectrometer (LA-ICP-MS) while individuals of *G. tumida* were analyzed via Inductively Coupled Plasma-Optical Emission Spectrometer (ICP-OES).

Due to their small mass size, *G. sacculifer* specimens were analyzed via laser ablation (Photon Machines Analyte.193 with HelEx sample cell) coupled with a Thermo ElementXS ICP-MS (LA-ICP-MS). Here we use similar preparation and analysis techniques as those developed by others(*41-43*). Prior to analysis, samples were sonicated in deionized water for 5-10 seconds, rinsed with methanol and dried. The final chamber was severed from the whole of the foraminifera and mounted onto carbon tape. Between

five to eight spots ~30 mm in diameter were analyzed for selected isotopes (^{11}B, ^{24}Mg, ^{25}Mg, ^{27}Al, ^{43}Ca, ^{44}Ca, ^{55}Mn, ^{66}Zn, ^{88}Sr) and integrated for a mean minor elemental signal. ^{27}Al, ^{55}Mn, ^{66}Zn were specifically monitored for clay and oxide contamination. Data acquisition was between 40-60s per spot analysis. NIST glass standards were analyzed at 4Hz and 4.1 laser fluence. Analytical reproducibility for NIST610 and NIST612 for Mg/Ca was 8.66 ± 0.14 and 1.31 ± 0.23 mmol/mol, respectively (1s, n = 359 over 25 analytical days). Carbonate standards and samples were analyzed at 4Hz and 1.13 laser fluence. Carbonate standard reproducibility for JCt-1-Plug and MACS-3 for Mg/Ca was 1.35 ± 0.15 and 7.61 ± 0.47 mmol/mol, respectively (1s, n=280 and 582). Specimens were analyzed from the inner shell surface to the outside to minimize surface heterogeneity during ablation. Average intra-test variability for Mg/Ca is 0.11 mmol/mol, which is comparable to a previous study(*42*). Eggins et al. (2003) have shown that LA-ICP-MS can reliably determine the range and variability of modern and Holocene temperature from a population of cold-dwelling and tropical planktonic foraminifera such as *G. sacculifer*. *Globigerinoides sacculifer* Mg/Ca values were converted to temperature using a Mg/Ca dissolution correction(*44*) and a multispecies temperature equation(*45*). $\Delta[CO_3^{2-}]$ values for the Mg/Ca dissolution correction were calculated using the GLODAP ocean carbon(*46*) and World Ocean Atlas temperature(*47*) datasets and estimated to be 5.69 mmol/kg and -13.06 mmol/kg for Site 806 and 849, respectively. Although $\Delta[CO_3^{2}]$ changes between the Holocene and LGM(*48*), we do not correct for them here.

Individual *G. tumida* specimens were analyzed via ICP-OES. Crushed individual *G. tumida* were rinsed and sonicated in Milli-Q and methanol, cleaned with reductive and oxidative reagents, and transferred into 1.5mL acid cleaned vials for a weak acid leach and final rinse before minor-element analysis(*49*, *50*). A PerkinElmer Optima 8300 ICP-OES was used to measure minor-element ratios(*51*). Long term Mg/Ca reproducibility for a liquid consistency standard and foraminifera standards are 3.318 ± 0.030 mmol/mol (1s, n=401) and 3.737 ± 0.181 mmol/mol (1s, n=103) respectively. Here we use the *G. tumida*-specific temperature calibration(*52*), which results in a good match between core-top estimated temperatures and local modern hydrographic data at ODP Sites 806 and 849.

Supplementary Text

Data Analysis: Quantile-Quantile (Q-Q) Plots

ENSO variability is not normally distributed because the El Niño phase is more extreme than the La Niña phase(*7*, *14*). Therefore, application of statistical tests that assume normality (e.g. standard deviation, variance) can lead to erroneous conclusions. Here we use a statistical visualization called a Q-Q (Quantile-Quantile) plot to compare the range and distribution of populations of individual foraminifera (described below). For reference, unaltered Mg/Ca data is plotted in Fig. S2.

Probability Density Functions (pdfs) are generated from each data set and indicate the probability that a sample taken at random will fall within a given distribution of temperature values (hereafter referred to simply as a *distribution*). As we are specifically interested in changes in seasonality and interannual variability, which typically impact the tails of a distribution, we are interested in how the tails of two distributions are different from one another. In a Q-Q plot (Fig. S3 for an example), the quantiles of each

probability distribution are plotted against each other; that is, the quantile of one distribution (from one sample) is on the horizontal axis and are plotted against the equivalent quantile of another distribution (from a different sample) on the vertical axis creating a series of points. If the mean and variability of two samples are the same, they plot along the one-to-one line. Changes in the mean, without changes in distribution, uniformly shifts the Q-Q series of points so that they are arranged in a line that is parallel to the one-to-one line. Changes in the distribution (e.g., standard deviation, skewness, kurtosis for normal distributions) pull the Q-Q series of points away from lines parallel to the one-to-one line. We estimate the uncertainty in distributions on these Q-Q plots using a Monte Carlo approach (Fig. S3 for an example), by resampling the cumulative distribution function (CDF) of the observed temperature distributions. Treating the CDF as a continuous function, it was resampled using random numbers to yield a dataset with the same number of temperatures as the original dataset. Quantiles in two percent increments (i.e. 50 bins) were then generated from the resampled datasets and plotted over the original data (see Fig. S3 for an example). This process was repeated 1000 times to produce an estimate of the variability in the Q-Q plot analysis due to sampling of the population distribution. The 90% confidence limits along the Y-direction were calculated for each quantile of the x-axis dataset, thus defining a 90% contour of the Monte Carlo distribution. In addition to the 1:1 line (grey dashed line), a mean adjusted 1:1 line (black dashed line) was also plotted to account for changes in the mean between the compared samples. Where the 1:1 line falls outside of the 90% confidence contours, this indicates the distributions are significantly different from one another at the 90% confidence limit.

Due to low numbers of individuals in some depth intervals, data from adjacent stratigraphic intervals were combined to increase the number of individuals in the Holocene-LGM comparison (Table S1). Prior to this combination, Q-Q plots and Monte-Carlo uncertainties of the separate samples were used to ascertain whether these adjacent depth intervals had similar temperature distributions. In these analyses the number of quantile bins was reduced to 25 because the number of individual foraminifera analyzed ranged from N= 26-70. These comparisons are shown in Figs. S3, S4, S5, S6 and S7 and demonstrate that samples that were combined for analysis have similar temperature distributions within sampling uncertainty.

Q-Q Plots of Modern Hydrographic Data

The ENSO signal in the modern hydrographic data at the locations of Sites 806 (Fig. S8 A/C) and 849 (Fig. S8 B/D) was manipulated in order to demonstrate how to extract information regarding changes in variability at different timescales from Q-Q plots. Monthly mean temperatures from 1958-2007 from the SODA v2.4 re-analysis dataset(*53*) were identified as Normal, El Niño or La Niña using the National Oceanic and Atmospheric Administration Climate Prediction Center's Oceanic Nino Index (ONI) applied to the Niño 3.4 SST time series. For the "No ENSO" trace (red), months identified as El Niño or La Niña were removed and replaced by the normal climatological monthly mean. In contrast, for the "Increased ENSO" (pink), months identified as El Niño or La Niña , the average amplitude of the excursion from the normal climatological mean was increased by 50%. Similarly, for the seasonality, the average seasonal excursion from the normal climatological mean was increased (blue) or decreased (turquoise) by 50% and added to the temperature. At Sites 806 and 849, manipulation of

the ENSO cycle clearly impacts the Q-Q trace, while changes in seasonality do not clearly impact the Q-Q trace (i.e. the distributions fall on or near the one-to-one line). Additionally, normal monthly means were manipulated to simulate decadal changes in seasonality (±1°C, e.g. Pacific Decadal Oscillation). Similar to changes in seasonality, simulated decadal variability has minimal impact on the Q-Q distribution (Fig. S9).

Comparison of Modern Hydrographic Data and Foraminifera Fluxes

Site 806: As a proxy for sea surface temperature (SST), the *G. sacculifer* derived temperature distribution from the core-top of Site 806 matches well with SODA hydrographic data at 15 m water depth. As a proxy for subsurface temperature, *G. tumida* derived temperature distributions are generally cooler and have a broader distribution than SODA hydrographic data at 97 m water depth. Though production and export for a certain season could explain temperature discrepancies, nearby sediment trap experiments indicate a relatively uniform export flux of *G. sacculifer* and *G. tumida* throughout the annual cycle(*54*). For *G. tumida*, a broad subsurface temperature range may be attributed to a depth habitat that is partially within the upper thermocline, (i.e., an environment with a strong temperature gradient). However, the benefit of comparing Holocene *G. tumida* temperature variability records to LGM *G. tumida* temperature variability records is that these potential biases are effectively minimized because they are inherent to both data sets.

Site 849: As a proxy for SST, the *G. sacculifer* derived temperature distribution from Site 849 is generally warmer than SODA hydrographic data at 15 m water depth. Nearby in the Panama Basin, sediment trap data indicates *G. sacculifer* has a maximum flux peak during summer months (June to September) with a secondary peak during winter (December to March)(*55*). Locally for Site 849, this flux pattern would result in a slight over-representation of moderate, not extreme warm, SSTs. Though *G. sacculifer* prefers warm temperatures and the minimum temperature recorded by *G. sacculifer* within this study is ~24˚C, *G. sacculifer* is known to precipitate shells within the EEP at ~21˚C(*56*). Consequently, the absence of cold temperatures during the glacial period is not due to biological limitation of *G. sacculifer*. As a proxy for subsurface temperature, *G. tumida* derived temperature distributions are generally cooler and have a normal distribution in comparison to the SODA hydrographic data at 97 m water depth, which is skewed toward warm subsurface temperatures due to fluctuations in thermocline depth likely related to ENSO(*57*). Though not specifically discussed in sediment trap data from the Panama Basin, nonspinose foraminifera, such as *G. tumida*, have a maximum flux during the season of maximum upwelling(*55*), which corresponds to moderately cool subsurface temperatures at Site 849. As with Site 806 we chose to compare Holocene and LGM distributions to minimize these biases.

The Impact of Bioturbation on Individual Foraminifera Datasets

Bioturbation of marine sediments, the process by which sediment is mixed by benthic organisms, impacts sedimentary records by mixing stratigraphically older sediments into younger horizons and somewhat vice versa. For individual foraminifera datasets reported here, the greatest concern is the possibility that individuals from the LGM may have mixed up into the late Holocene horizon(*58*) thus artificially enhancing late Holocene variability. Stott and Tang (1996) showed probable contamination of $\delta^{18}O$ enriched LGM

individuals into Holocene samples. This impacts the overall surface temperature reconstructions by potentially minimizing the true magnitude of temperature change and enhancing Holocene $\delta^{18}O$ variability. The $\delta^{18}O$ values of individual foraminifera are impacted by both ice volume and temperature change. In the Stott and Tang (1996) study, the ice volume signal accounts for nearly 2/3 of the $\delta^{18}O$ shift from the Holocene to the LGM. In contrast, our study uses the Mg/Ca of individual foraminifera which primarily records temperature. Consequently, the impact on variability due to the contamination of LGM individuals into the Holocene sample for individual Mg/Ca analyses is much smaller than the individual $\delta^{18}O$ analyses used in the Stott and Tang (1996) study. Additionally, the degree of smoothing of marine records by bioturbation is proportional to the sedimentation rate. As the sedimentation rates at our study sites are nearly twice the sedimentation rates for the box cores used in the Stott and Tang (1996) study, bioturbation is likely to be less of an issue at our study locations. Nevertheless, as the Late Holocene variability is significantly higher than the LGM variability at Site 849, possible mixing from bioturbation has the greatest impact on our interpretation at this location.

To examine the possible impact of mixing LGM individuals up into the Late Holocene at Site 849, we carried out the following sensitivity test: the four coldest individuals from the LGM were added twice to the original Late Holocene population to create an altered Late Holocene population. That is, eight cold LGM individuals were added to the Late Holocene population to see the possible impact of bioturbation "contamination" on the Q-Q plot distributions (Fig. S10). This sensitivity test roughly approximates the number of LGM individuals "contaminating" the Holocene samples in the Stott and Tang (1996) study and simulates the maximum alteration possible. For completeness, we repeated this experiment with the four warmest individuals from the LGM (Fig. S10). The addition of cold or warm LGM individuals does not significantly affect the distribution of the original Late Holocene population. Additionally, the "bioturbated" Late Holocene population compared to the LGM population has essentially the same distribution as the original Late Holocene population compared to the LGM population. Consequently, the impact of bioturbation on our distributions and interpretations is likely to be minimal.

Reanalysis of Previously Published Individual Foraminifera Datasets

Using the Q-Q analysis described above, we reevaluated previously published individual foraminifera datasets to construct a coherent picture of possible changes in ENSO variability during the LGM. To compare the published datasets to each other, and to interpret them within the context of our study, we consider choice of location (Fig. S11), choice of foraminiferal species, and possible impact of changes in the mixed layer and thermocline on individual foraminifera SST distributions.

Koutavas and Joanides (2012)

Koutavas and Joanides (2012) generated individual foraminifera $\delta^{18}O$ data at a site in the far EEP and interpreted their data as indicating that ENSO variability was enhanced in the LGM compared to the Late Holocene. However, consideration of the hydrographic variability at their site supports an alternative interpretation that is complementary with our study. Koutavas and Joanides (2012) generated $\delta^{18}O$ values from individual *G. ruber* shells at core V21–30 (1° 13′S, 89° 41′W, 617 m depth) and use variance as a measure of

ENSO variability. However, at this site, seasonality and ENSO impact variance equally and variance is a poor measure of ENSO variability. Here we reanalyze the Koutavas and Joanides (2012) dataset using the Q-Q methods described above.

Globigerinoides ruber is a shallow mixed-layer species and average core-top $\delta^{18}O$ values from Koutavas and Joanides (2012) are consistent with a calcification depth of ~5 m. Modern hydrographic data at 5 m depth was converted to $\delta^{18}O_{calcite}$ for further Q-Q comparison. First, $\delta^{18}O_{water}$ was estimated using the gridded $\delta^{18}O$ database and salinity-$\delta^{18}O_{water}$ relationship of (*59*) combined with salinity values from the SODA dataset. Second, these $\delta^{18}O_{water}$ estimates and SODA v2.4 monthly mean temperatures were converted to $\delta^{18}O_{calcite}$ using the paleotemperature equation of (*60*). In Fig. S12A, altered modern hydrographic data show that changes in seasonality have a stronger impact on the warm and cold tails of the distribution than ENSO. Our Q-Q plots of the $\delta^{18}O$ values from glacial *G. ruber* samples compared to the core-top sample from core V21–30 provide little support for a change in distribution (Fig. S13). In general, the $\delta^{18}O_{calcite}$ values plot on an offset, one-to-one line and indicate there was no change in $\delta^{18}O_{calcite}$ distribution between the Late Holocene and LGM and glacial intervals. Similar results for other Late Holocene intervals compared to LGM and glacial intervals were also found (figures not shown).

Recent statistical analyses by (*22*) suggest that $\delta^{18}O$-based temperature variability reconstructions from *G. ruber* from core V21–30 used in the Koutavas and Joanides (2012) study are not likely to identify changes in ENSO, but are likely to capture changes in seasonality. A robust result among climate models that simulate ENSO activity indicates there is an inverse relationship between the seasonal cycle and ENSO (*3*, *61*). For example when ENSO intensity decreases, the seasonal cycle increases. We suggest the robust decrease in variability during the LGM in comparison to the late Holocene recorded at Site 849 (e.g., Figure S3, this study) is masked at V21-30 by an increase in seasonality. That is, the decrease in ENSO strength found at Site 849 is not detectable at V21-30 because seasonality increased, thereby offsetting the decrease from ENSO. Therefore we interpret the $\delta^{18}O$ data at site V21-30 Koutavas and Joanides (2012) to indicate enhanced seasonality during the LGM in comparison to the late Holocene.

Sadekov et al. (2013)

Sadekov et al. (2013) generated $\delta^{18}O$- and Mg/Ca-based variability reconstructions at a site in the far EEP, south of the study of Koutavas and Joanides (2012). Although they interpreted their data as greater ENSO variability during the LGM in comparison to the Late Holocene, consideration of their choice of species and changes in the LGM thermocline supports an alternative interpretation that is consistent with our *G. tumida* data from Site 849. In their study, they generated $\delta^{18}O$ and Mg/Ca values from repetitive measurements of 2-3 *Neogloboquadrina dutertrei* shells to reconstruct subsurface variability at site CP38-17P (1° 21′S, 90° 15′W, 2580 m depth) within the cold tongue. However, multispecies stable isotope reconstructions of the upper water column suggest the mixed layer was thicker and the thermocline was deeper in the eastern Pacific cold tongue during the LGM in comparison to today(*24*, *25*, *62*). These thermocline changes affect interpretations of subsurface variability reconstructions from foraminifera. Here we

reanalyze the Sadekov et al. (2013) dataset using the Q-Q methods described above (Fig. S14 and S15).

Within the cold tongue region, *N. dutertrei* has a deep calcification depth and average core-top $\delta^{18}O$ values from Sadekov et al. (2013) are consistent with a calcification depth of ~120 m. As the Sadekov et al. (2013) study uses both Mg/Ca and $\delta^{18}O$ values of *N. dutertrei*, we compare the Mg/Ca values to altered SODA v2.4 monthly mean temperatures (see Q-Q Plots of Modern Hydrographic Data above) and $\delta^{18}O$ values to modern hydrographic data converted to $\delta^{18}O_{calcite}$ (see Koutavas and Joanides section above) at 112 m depth. In Figs. S12 B and D, altered modern hydrographic data show that changes in ENSO have a strong impact on the warm end of the distribution whereas seasonality has little influence on the distribution. Our Q-Q plots of Sadekov et al.'s $\delta^{18}O$ (Fig. S14) and Mg/Ca (Fig. S15) values from glacial *N. dutertrei* shells compared to the core-top suggest enhanced variability during the LGM in comparison to the Late Holocene (though not statistically significant). This is similar to our observation using Mg/Ca derived temperature values of *G. tumida* at Site 849. Site CP38-17P (Sadekov et al., 2013) and Site 849 (this study) are similarly located in the EEP cold tongue where the thermocline is shallow and steep. Although enhanced variability could be consistent with an increase in ENSO (Fig. S12 B and D), known changes in the upper ocean structure within the EEP cold tongue(*24*, *25*, *62*) complicate this interpretation.

Within the EEP cold tongue, *N. dutertrei* and *G. tumida* calcify within the lower portion of the thermocline(*26*, *40*) where there is a relatively small temperature change with depth, and therefore small changes in the depth of the thermocline results in relatively small variability in recorded temperatures. The enhanced variability during the LGM recorded by *N. dutertrei* and *G. tumida* within the EEP cold tongue is likely an artifact of a thicker mixed layer and deeper thermocline during the LGM in comparison to the Late Holocene. During the LGM, *N. dutertrei* and *G. tumida* were likely calcifying within the upper thermocline where there is a relatively large temperature change with depth. Therefore, small movements of the thermocline resulted in an apparent increase in variability during the LGM in comparison to the Late Holocene. Futhermore, the lack of cooling in the measurements on LGM *N. dutertrei* and *G. tumida* subsurface species is consistent with this interpretation: calcification in upper, warmer thermocline waters would counteract any LGM cooling. Alternatively, in the modern ocean, subsurface variability in the EEP thermocline is forced locally and remotely by seasonal winds(*57*); hypothetically, higher subsurface variability could indicate increased seasonal vertical migration of the thermocline, responding to increased seasonal variations in winds during the LGM in comparison to the Late Holocene. However, changes in thermocline structure are more likely to be driving the changes in subsurface variability reconstructions seen within the EEP during the LGM in comparison to the Late Holocene.

While thermocline variability is strongly associated with modern ENSO events(*63*), a thicker mixed layer and deeper thermocline within the cold tongue during the LGM complicate ENSO interpretations that are based on subsurface variability reconstructions alone. Sea surface variability reconstructions from locations with strong ENSO signals, separate from changes in seasonality, like those at Site 849 (this study) may provide a more straightforward record of ENSO variability through time.

Leduc et al. (2009)

Leduc et al. (2009) generated individual foraminifera $\delta^{18}O$ values at a site in the Eastern Pacific Warm Pool (EPWP). Consistent with our study, they interpreted their data as indicating that ENSO variability was reduced during the LGM compared to the Late Holocene. In their study, they generated $\delta^{18}O$ values from *N. dutertrei* at site MD 02-2529 (8° 12′N, 84° 07′W, 1619 m depth) and use variance as a measure of ENSO. We reanalyze the Leduc et al. (2009) dataset using the Q-Q methods described above to determine whether their findings are robust using the same methodology as in our study.

Neogloboquadrina dutertrei is known to shift its depth habitat, preferring a shallow depth habitat in places with a well-defined shallow thermocline such as the EPWP(*27*, *40*) and a deeper habitat in places such as the EEP. Average core-top $\delta^{18}O$ values from Leduc et al. (2009) are consistent with a calcification depth of ~50 m. Because the Leduc et al. (2009) study uses $\delta^{18}O$ values of *N. dutertrei*, modern hydrographic data at 58 m depth was converted to $\delta^{18}O_{calcite}$ for further Q-Q comparison (see Koutavas and Joanides section above). In Fig. S12C, altered modern hydrographic data show that changes in ENSO have a strong impact on the warm and cold ends of the distribution whereas seasonality has little influence on the distribution. Our Q-Q plots of the $\delta^{18}O$ values from glacial *N. dutertrei* compared to the core-top suggest reduced variability during the glacial period in comparison to the Late Holocene (Fig. S16). This is consistent with a reduction in ENSO (Fig. S12C) during the LGM in comparison to the Late Holocene, and agrees with the original interpretation of Leduc et al. (2009).

Though upper ocean structure changed within the cold tongue(*24*, *25*, *62*), the mixed layer and thermocline depth in the EPWP was relatively stable: ice-volume corrected $\delta^{18}O$ values from Leduc *et al*. suggest the subsurface was ~2˚C (~0.5‰) cooler during the LGM in comparison to the Late Holocene, which is similar in magnitude to previously published sea surface temperature estimates for the EPWP region from multiple sites and proxies (~2.3˚C, see Western Equatorial and Eastern Equatorial Pacific SST Gradients section below). These data indicate *N. dutertrei* maintained its calcification position with respect to the thermocline and therefore, unlike in the EEP cold tongue, was not impacted by LGM thermocline adjustments.

Leduc et al. show *N. dutertrei* lives in a zone of significant thermocline variability related to ENSO in the modern ocean, which is also seen in the Q-Q plots of modern hydrographic data (Fig. S12C). The $\delta^{18}O$ values from individual *N. dutertrei* show reduced thermocline variability, suggesting a reduction in ENSO during the glacial period in comparison to the Late Holocene (Leduc et al., 2009).

In summary, our re-analysis of previous individual foraminifera studies suggests that during the LGM (1) reduced variability in locations and species sensitive to ENSO, (2) increased variability in locations and species sensitive to the seasonal cycle and (3) increased variability in locations and species affected by a deep thermocline unrelated to ENSO. Together these data indicate a reduction in ENSO variability and increased seasonality during the LGM.

Western Equatorial and Eastern Equatorial Pacific SST Gradients

Previous authors have suggested a strong inverse relationship between the zonal SST gradient between the WEP and EEP and ENSO variability(*11*, *12*) in that when the gradient is strong, ENSO is weak. Here we evaluate our variability reconstructions with respect to spatial changes in SST and WEP-EEP zonal SST reconstructions during the LGM and Late Holocene. We synthesized previously generated SST records [Table S3, (*27*, *28*, *39*, *64-70*)] and employ a time slice from the Holocene (4-6 ka) and Last Glacial Maximum (18-20 ka). Using the published age models, and Mg/Ca- and Uk'37-derived temperatures, we calculated the temperature difference from the LGM to Holocene for the WEP, EPWP and EEP, which are plotted on the modern SST field (Fig. S17). We find the WEP and EPWP had a similar magnitude of cooling between the LGM and Late Holocene (~2.7 and 2.3˚C, respectively) while the cold tongue cooled by only ~1.6˚C. Overall, the zonal temperature gradient between the WEP and EEP was reduced and our single foraminifera results suggest reduced ENSO variability during the LGM in comparison to the Late Holocene. Therefore, our analysis does not support a strong inverse relationship between ENSO strength and the zonal temperature gradient. Instead our analysis is consistent with recent modeling results showing weaker ENSO when the zonal SST gradient is reduced(*29*).

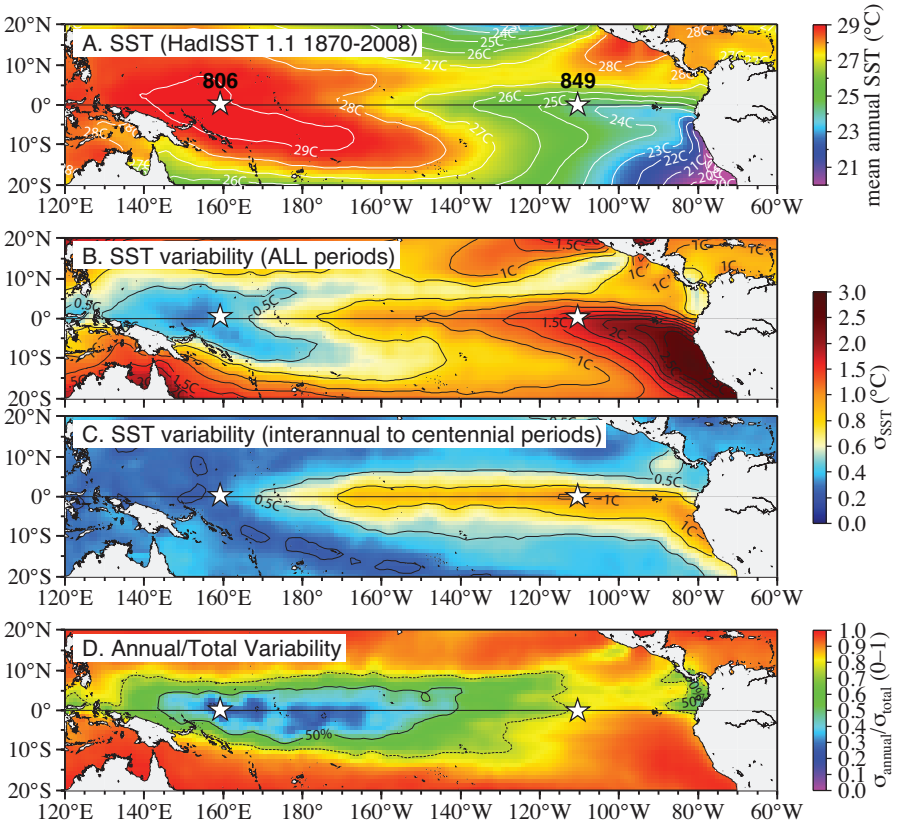

Fig. S1.
Modes of Variability in the Tropical Pacific. Mean annual sea surface temperatures (calculated from Rayner et al., 2003) (A). Variability (standard deviation) of monthly sea surface temperatures 1870 – 2008 (B) and of monthly values with the annual cycle removed (C), and the proportion of total SST variability due to the annual cycle (D). Cool colors in (D) are regions dominated by interannual to centennial variations while warm colored regions are dominated by the annual cycle.

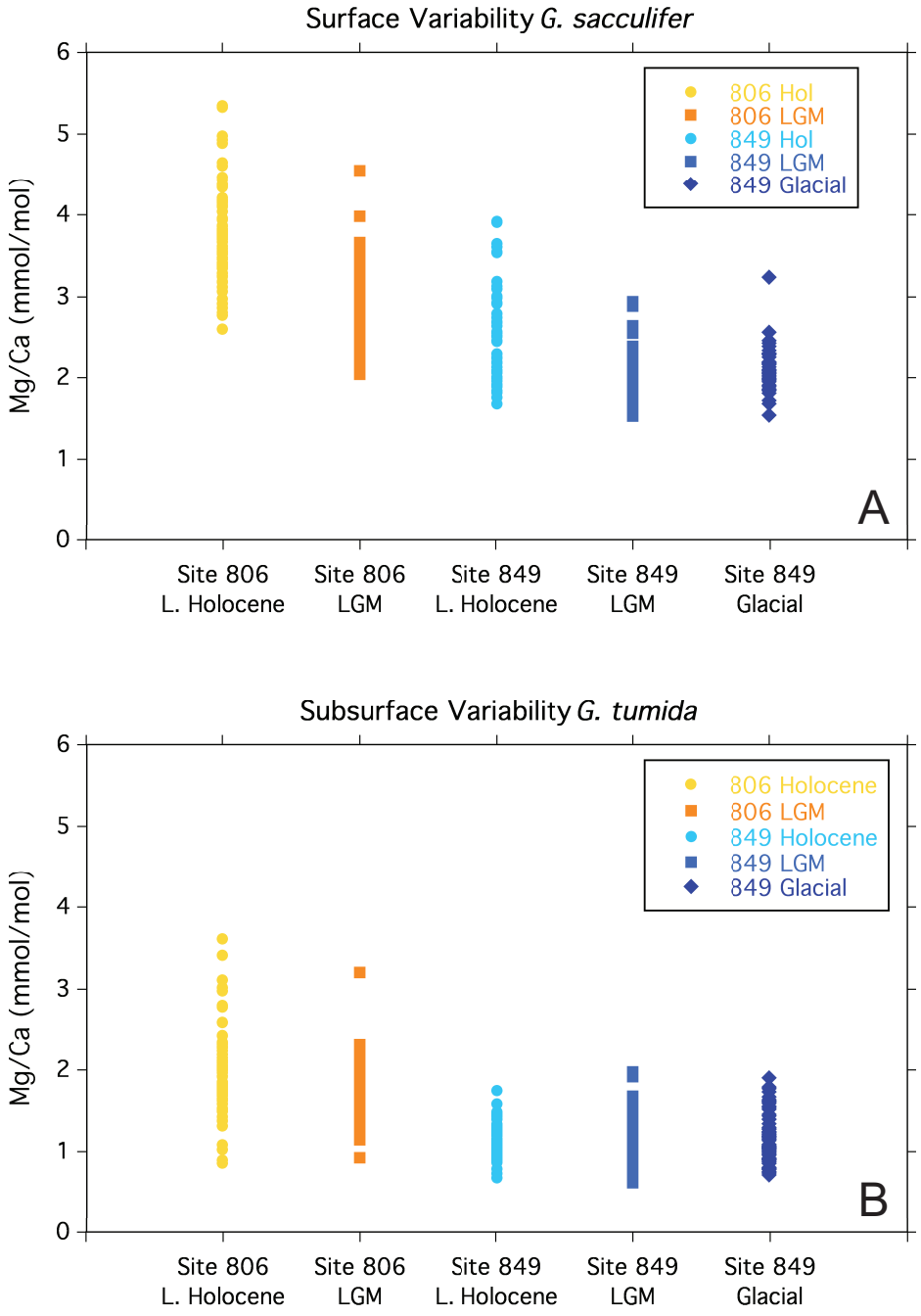

Fig. S2

Mg/Ca (mmol/mol) values of *G. sacculifer* and *G. tumida* from the WEP and EEP. *G. sacculifer* Mg/Ca values were collected via LA-ICP-MS while *G. tumida* Mg/Ca values were collected via ICP-OES.

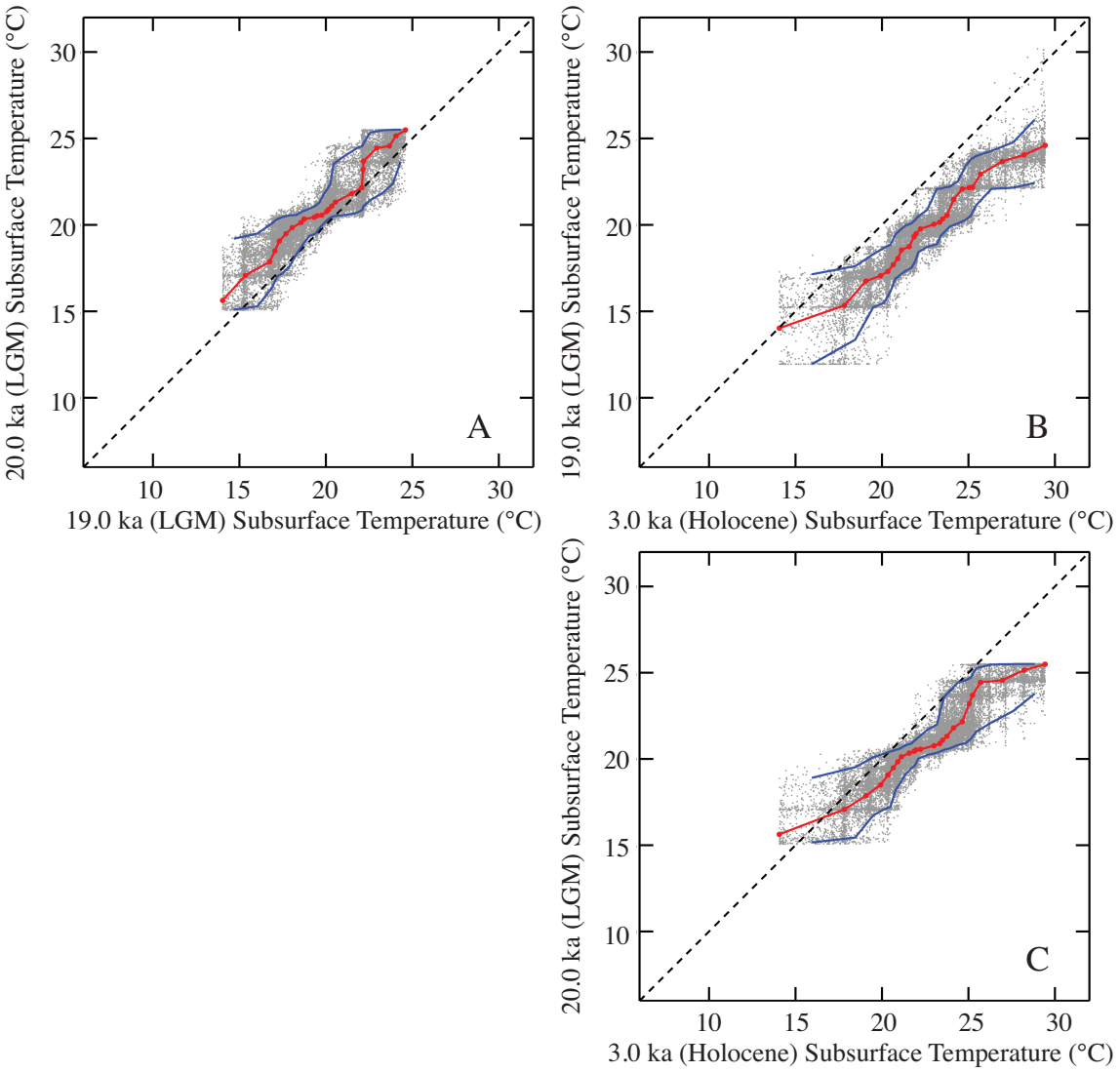

Fig. S3

Q-Q plots for subsurface dwelling *G. tumida* from the WEP. Depth intervals 0-2 cm (~3 ka, Holocene), 51-53 cm (~19 ka, LGM) and 53-55 cm (~20 ka, LGM) from ODP Site 806 are compared in Q-Q plots. Cumulative distribution function (red line), Monte Carlo resampling (grey dots) and 90% confidence limits (blue lines) are shown. When the LGM samples are compared to each other (A) there is little difference in the distributions between the two populations. Similarly, when the LGM samples are compared to the Holocene sample (B and C), they have comparable distributions. Therefore, the two LGM samples are aggregated and compared to the Holocene sample.

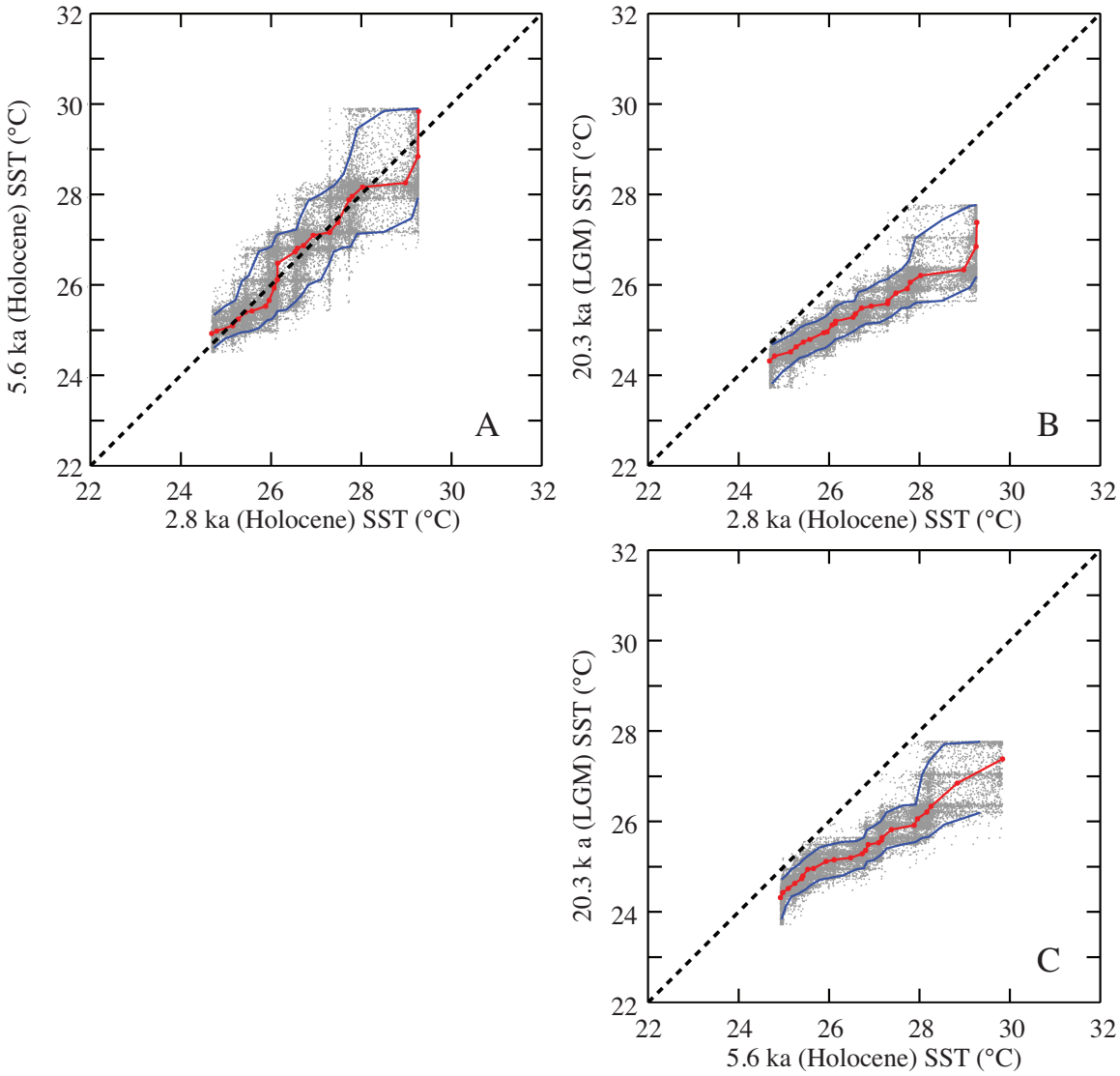

Fig. S4

Q-Q plots for surface dwelling *G. sacculifer* from the EEP Holocene and LGM, Depth intervals 6-8 cm (2.8ka, Holocene), 15-18 cm (5.6ka, Holocene), and 74-80 cm (20.3ka, LGM) from ODP Site 849 are compared (symbols and colors as in Fig. S3). When the Holocene samples are compared to each other (A) there is little difference in the distributions between the two populations. Similarly, when the Holocene samples are compared to the LGM sample (B and C), they have comparable distributions. Therefore, the two Holocene samples are aggregated and compared to the LGM sample.

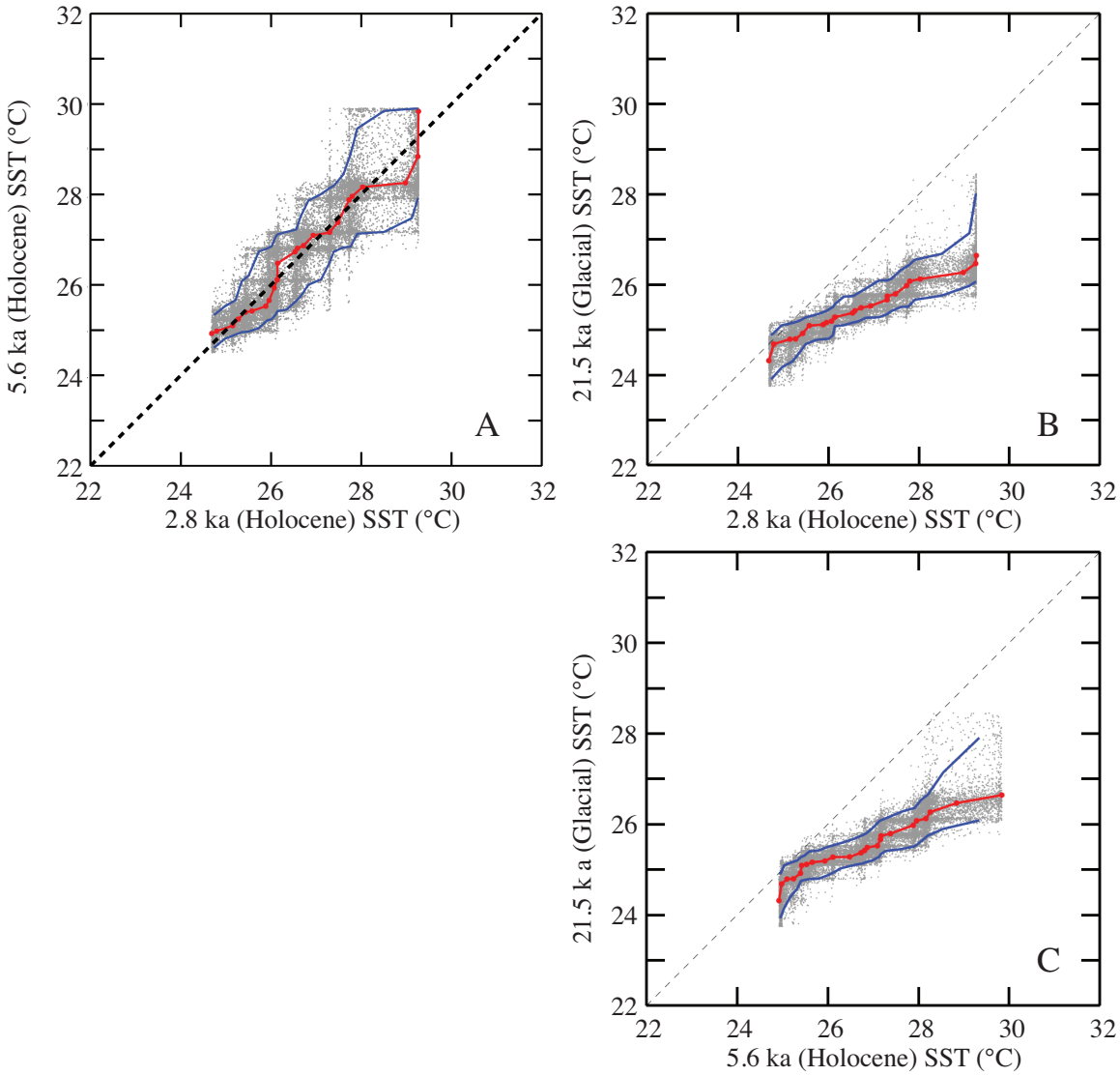

Fig. S5

Q-Q plots for surface dwelling *G. sacculifer* from the EEP Holocene and Glacial. Depth intervals 6-8 cm (2.8ka, Holocene), 15-18 cm (5.6ka, Holocene), and 85-87 cm (21.5ka, glacial) from ODP Site 849 are compared (symbols and colors as in Fig. S3). When the Holocene samples are compared to each other (A) there is little difference in the distributions between the two populations. Similarly, when the Holocene samples are compared to the glacial sample (B and C), they have comparable distributions. Therefore, the two Holocene samples are aggregated and compared to the glacial sample.

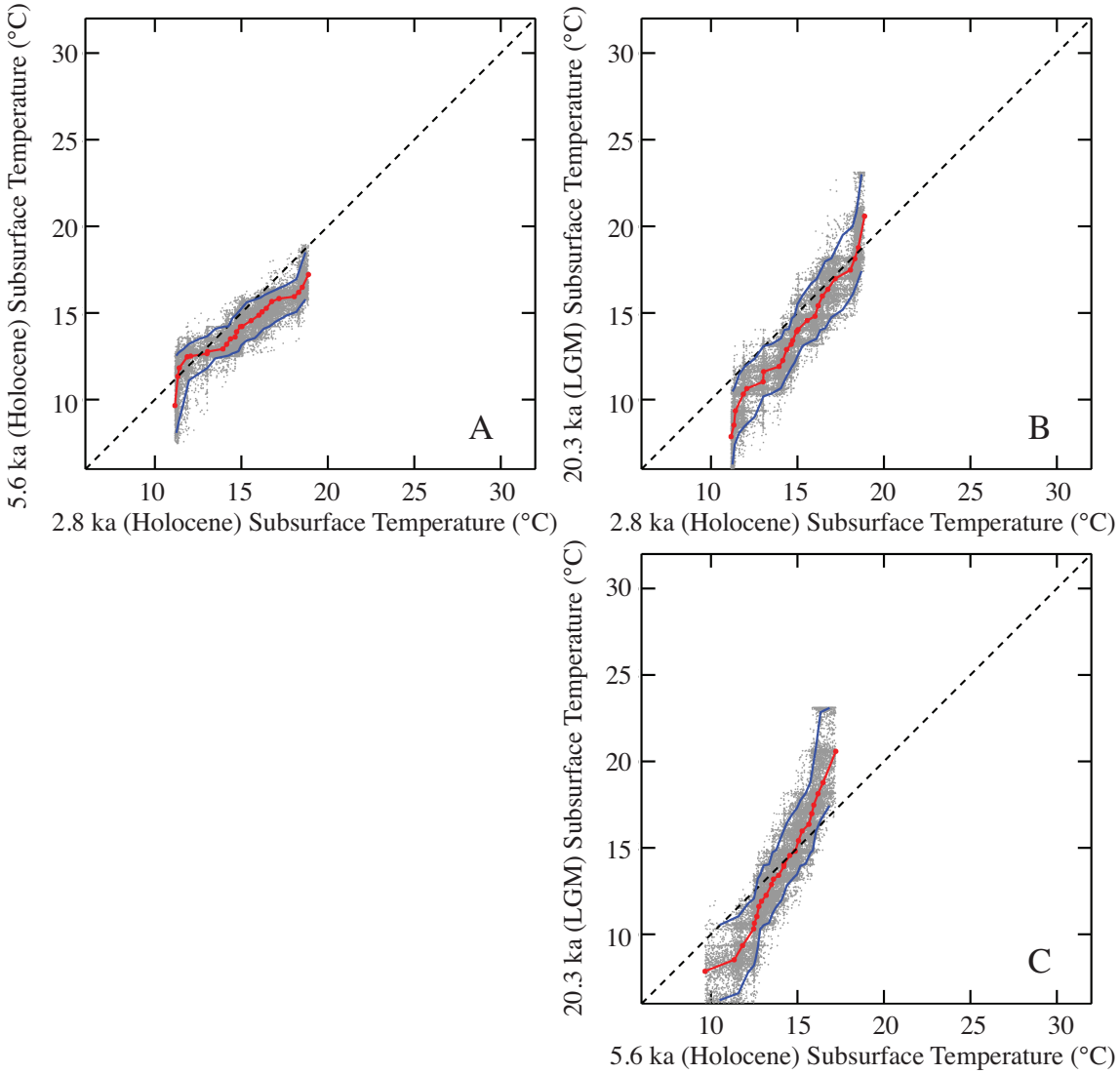

Fig. S6

Q-Q plots for surface dwelling *G. tumida* from the EEP Holocene and LGM. Depth intervals 6-8 cm (2.8ka Holocene), 15-18 cm (5.6ka, Holocene), and 74-80 cm (20.3ka, LGM) from ODP Site 849 are compared (symbols and colors as in Fig. S3). When the Holocene samples are compared to each other (A) there is little difference in the distributions between the two populations. Similarly, when the Holocene samples are compared to the LGM sample (B and C), they have comparable distributions. Therefore, the two Holocene samples are aggregated and compared to the LGM sample.

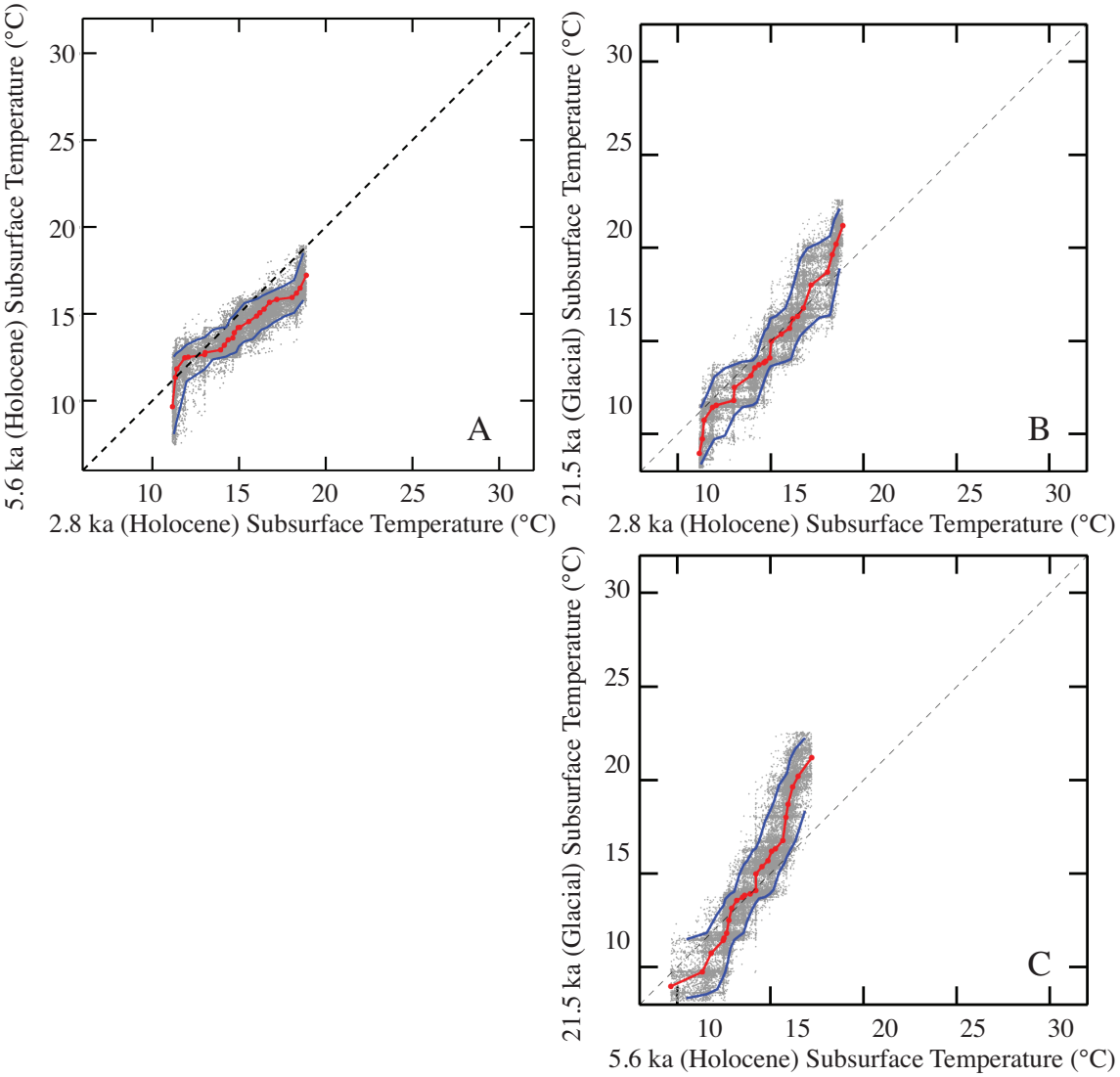

Fig. S7

Q-Q plots for surface dwelling *G. tumida* from the EEP Holocene and Glacial. Depth intervals 6-8 cm (2.8ka, Holocene), 15-18 cm (5.6ka, Holocene), and 85-87 cm (21.5ka, glacial) from ODP Site 849 are compared (symbols and colors as in Fig. S3). When the Holocene samples are compared to each other (A) there is little difference in the distributions between the two populations. Similarly, when the Holocene samples are compared to the glacial sample (B and C), they have comparable distributions. Therefore, the two Holocene samples are aggregated and compared to the glacial sample.

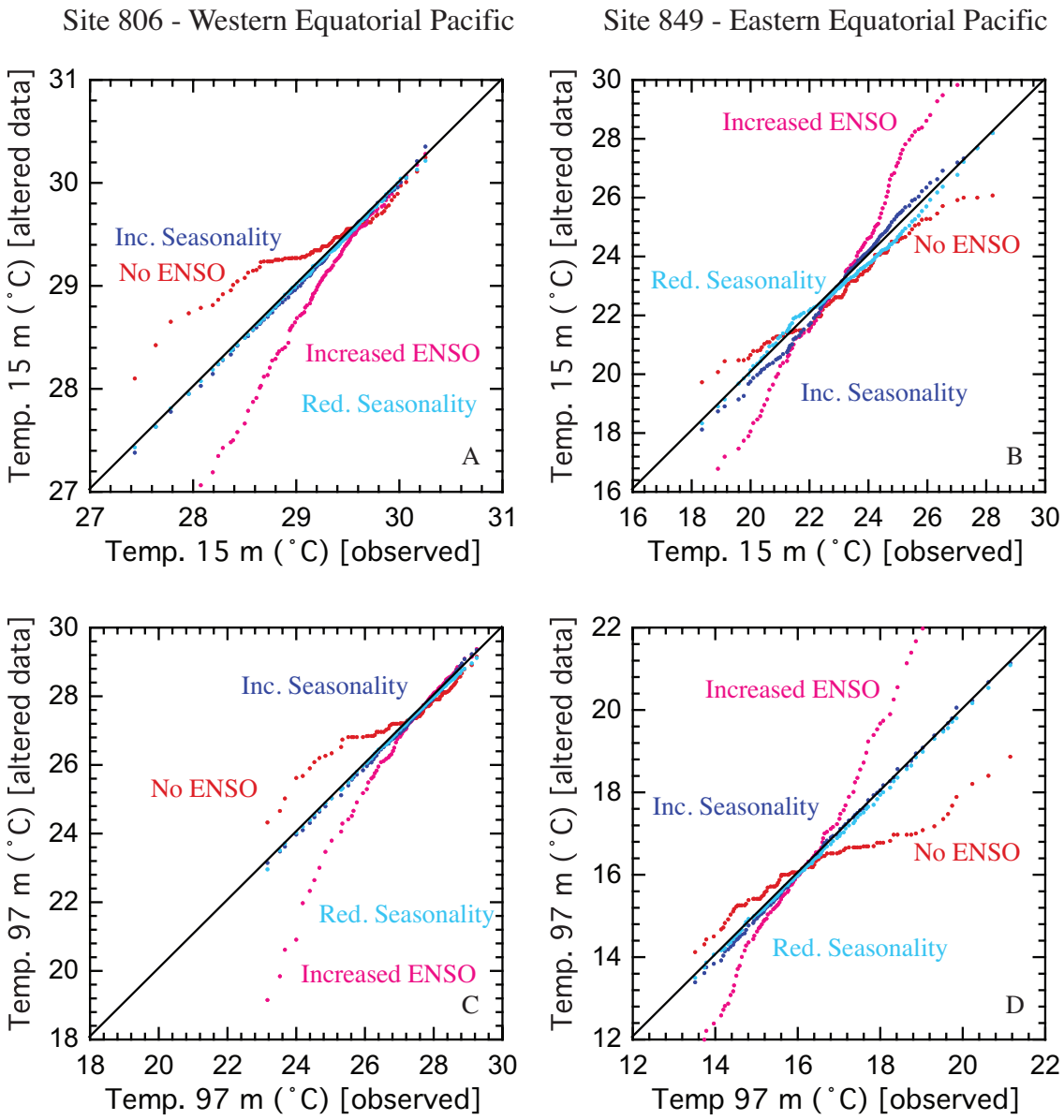

Fig. S8

Q-Q plots of altered modern hydrographic data at the locations of Sites 806 and 849. SODA v2.4 average monthly means are manipulated with increased ENSO (pink), no ENSO (red), increased seasonality (blue) and reduced seasonality (turquoise). WEP Site 806 surface (15 m, A) and subsurface (97 m, C). EEP Site 849 surface (15 m, B) and subsurface (97 m, D).

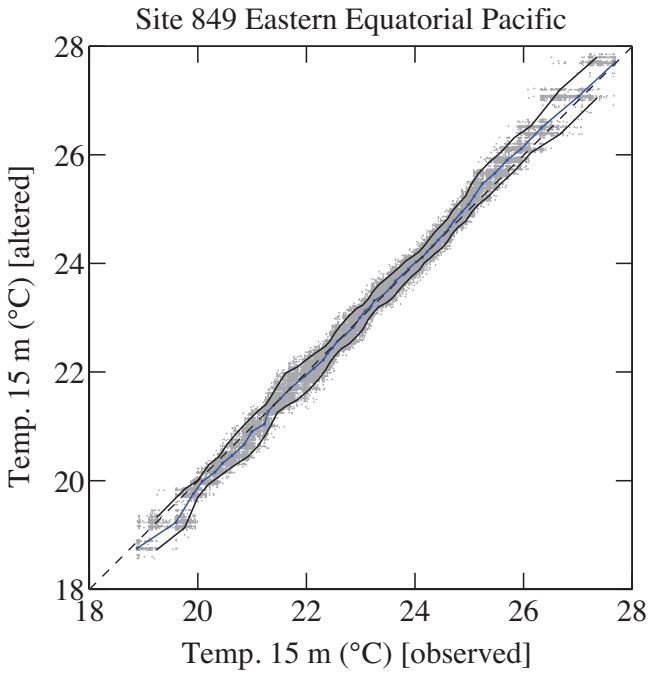

Fig. S9

Q-Q plots of altered surface modern hydrographic data at the location of Site 849 that simulate changes to decadal variability. SODA v2.4 average non-ENSO monthly means are manipulated to simulate decadal changes in seasonal variability (±1°C). Similar to changes in seasonality, simulated decadal variability has minimal impact on the Q-Q distribution.

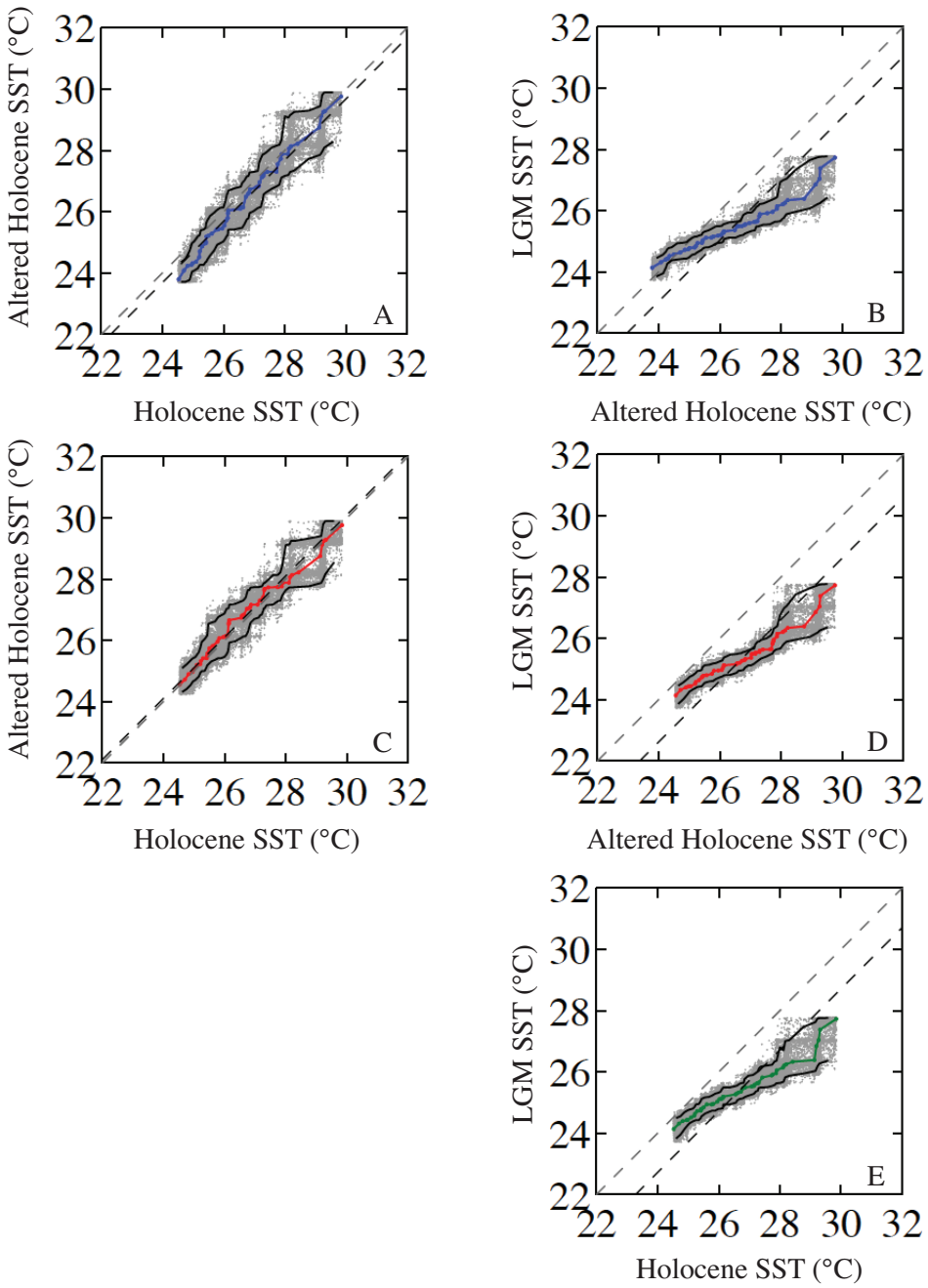

Fig. S10

Q-Q plots of the simulated impact of bioturbation on Late Holocene distributions. Cold (blue) and warm (red) individuals from the LGM population were added to the Late Holocene to create an altered Late Holocene distribution. There is no significant change in distribution between the original Late Holocene and altered late Holocene populations (A,C). Additionally, the altered Late Holocene population compared to the LGM population has a similar distribution (B,D) to the original Late Holocene population compared to the LGM population (green, E) suggesting minimal impact of bioturbation on the Q-Q plots distributions reported in this study.

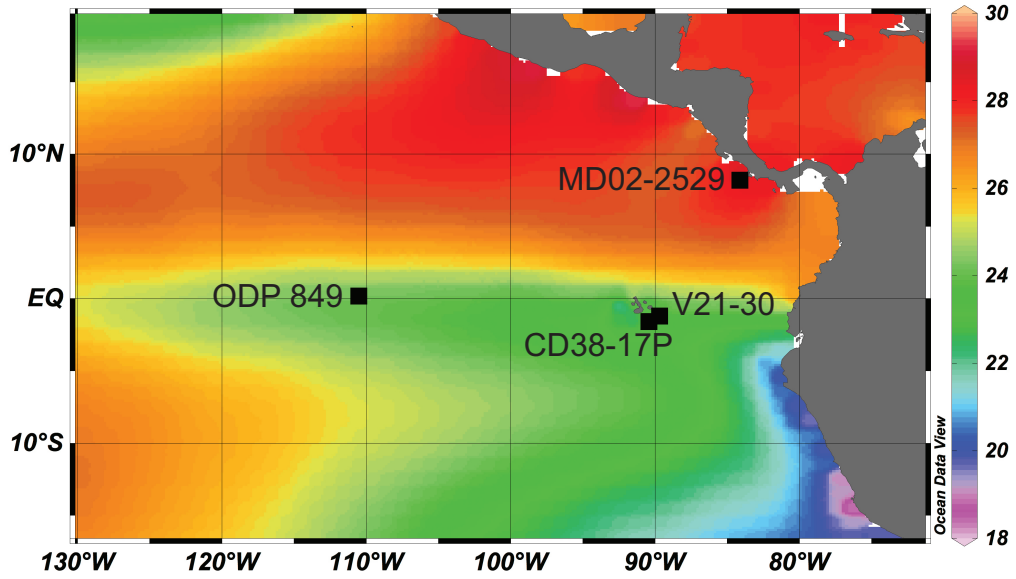

Fig. S11

Sea surface temperatures in the eastern equatorial Pacific with the location of our study site (ODP 849) and previously published individual foraminifera study sites [V21-20: Koutavas and Joanides, (2012); CD38-17P: Sadekov et al. (2013); and MD02-2529: Leduc et al. (2009)].

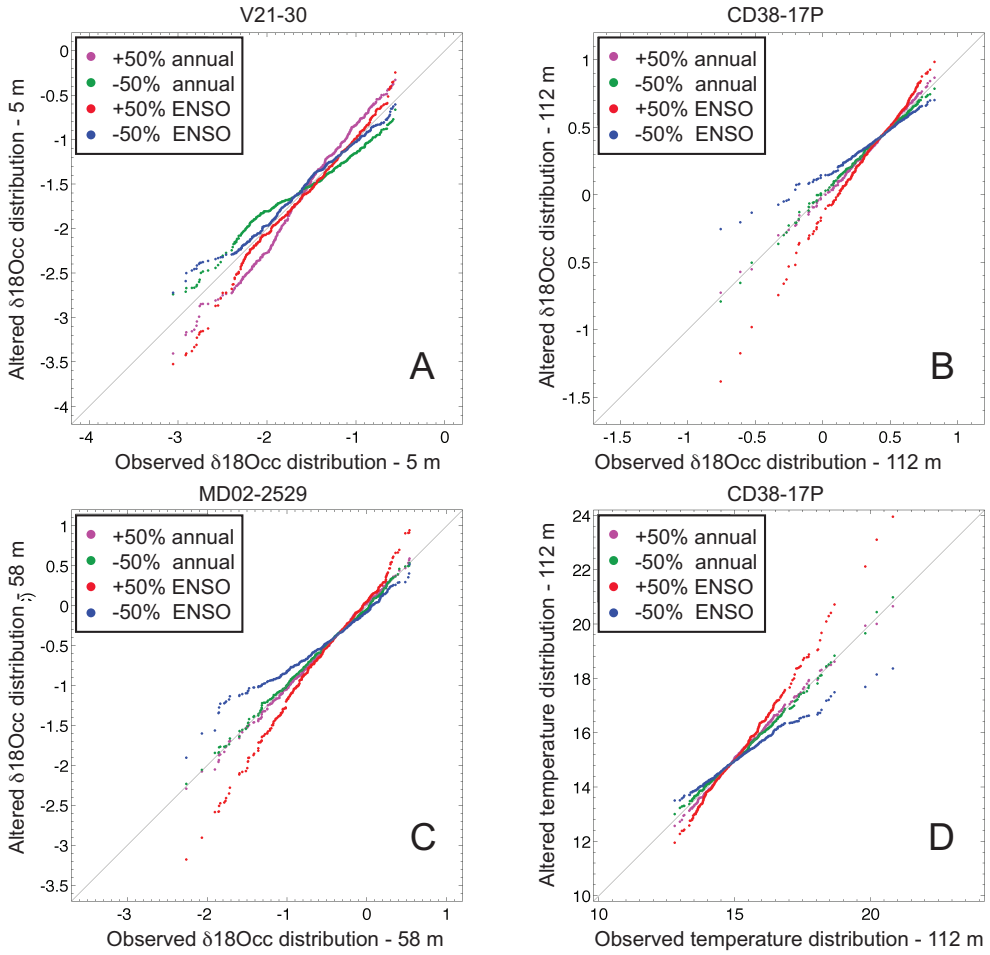

Fig. S12

Q-Q plots of altered modern hydrographic data at the locations of Sites V21-30, CD38-17P and MD02-2529 used in respectively, Koutavas and Joanides, (2012), Sadekov et al. (2013) and Leduc et al. (2009). SODA v2.4 average monthly means are altered with increased ENSO (red), no ENSO (blue), increased seasonality (purple) and reduced seasonality (green). For comparison to individual foraminifera $\delta^{18}O$ values, SODA v2.4 average monthly means were converted to $\delta^{18}O$ values as described in the text (A, B and C). As Sadekov et al. (2013) also measured the Mg/Ca of individual foraminifera as a proxy for temperature, the manipulated temperature monthly means are plotted in D.

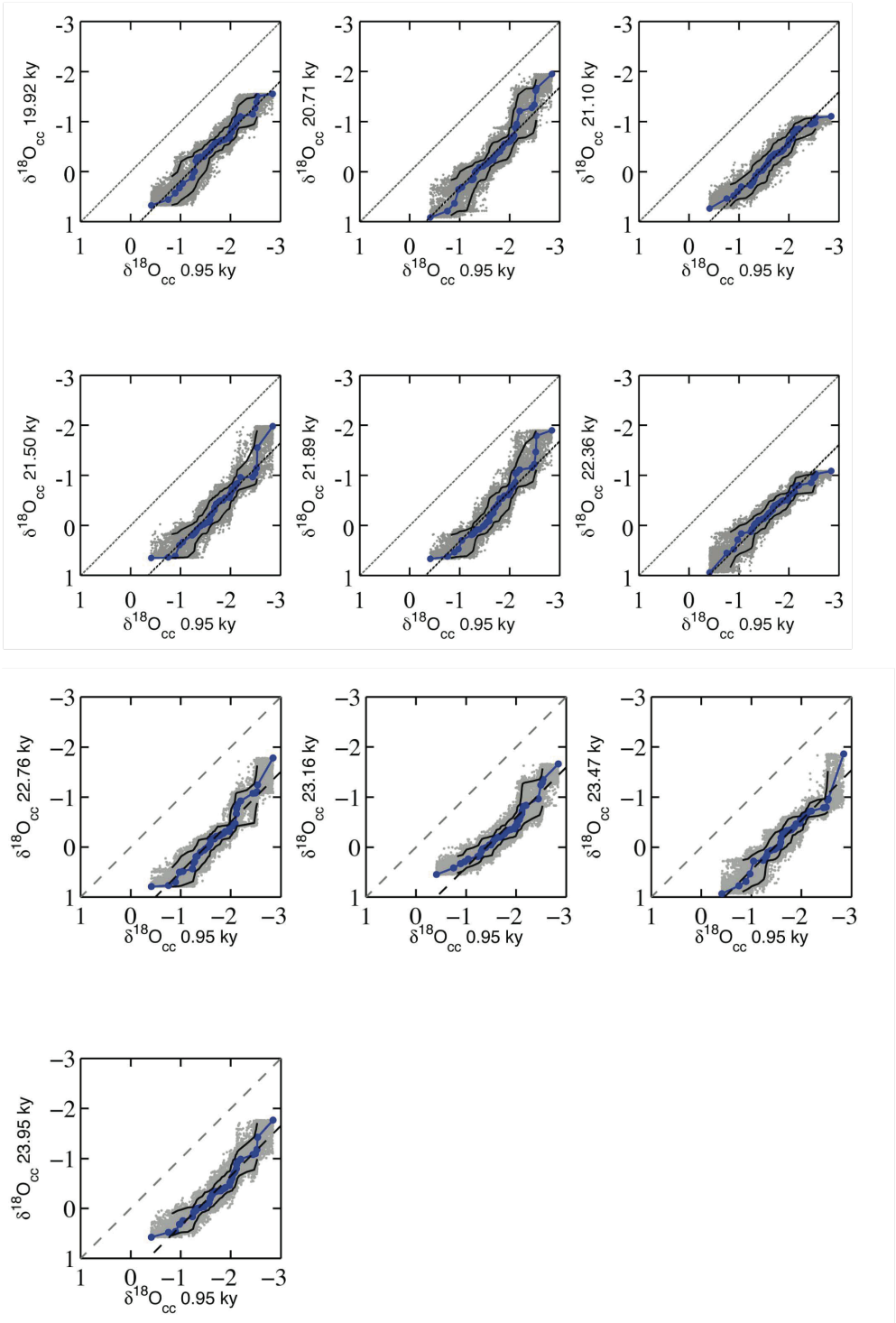

Fig. S13

Q-Q plots of Koutavas and Joanides (2012) $\delta^{18}O$ values of individual *G. ruber* from the Late Holocene core top in comparison to LGM and glacial intervals. Resampling of pdf distribution (blue line), Monte Carlo simulation (grey dots) and mean adjusted one-to-one line (black line).

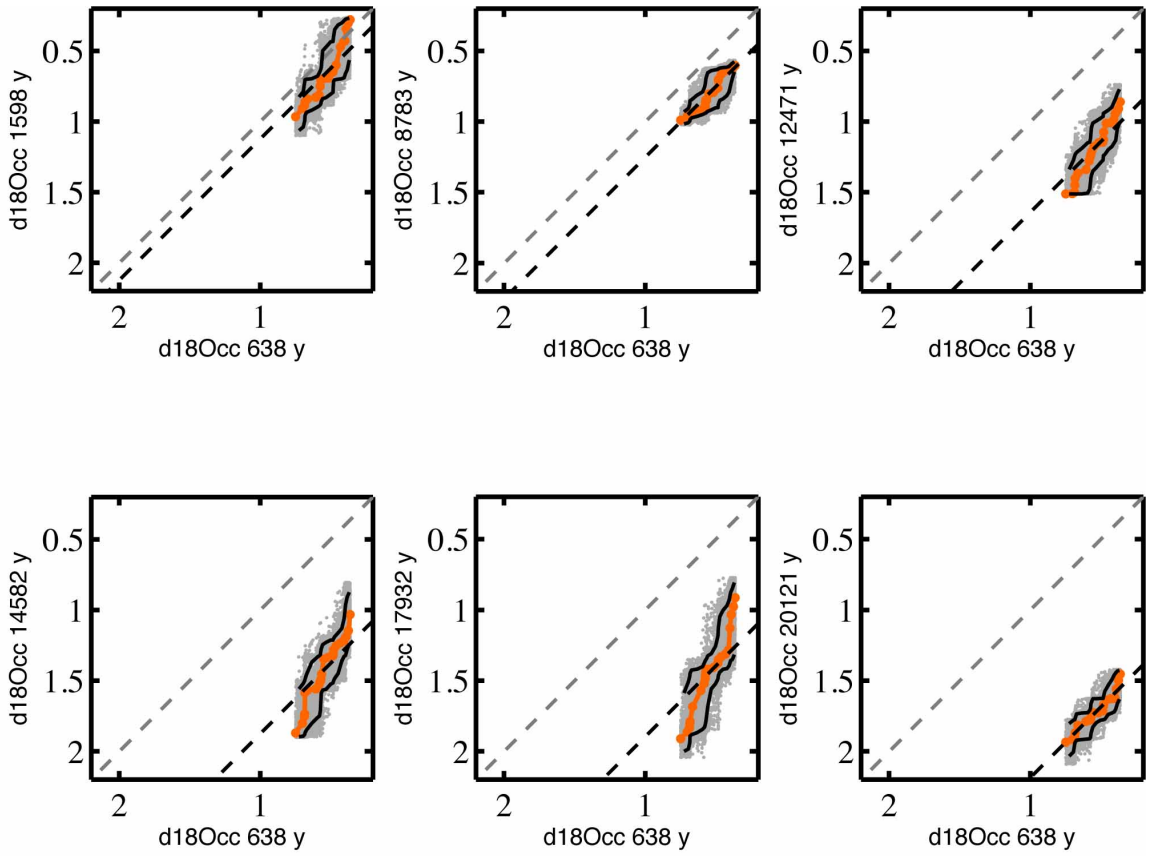

Fig. S14

Q-Q plots of Sadekov et al. (2013) $\delta^{18}O$ values of individual *N. dutertrei* from the Late Holocene core top in comparison to LGM interval. Resampling of pdf distribution (orange line), Monte Carlo simulation (grey dots) and mean adjusted one-to-one line (black line).

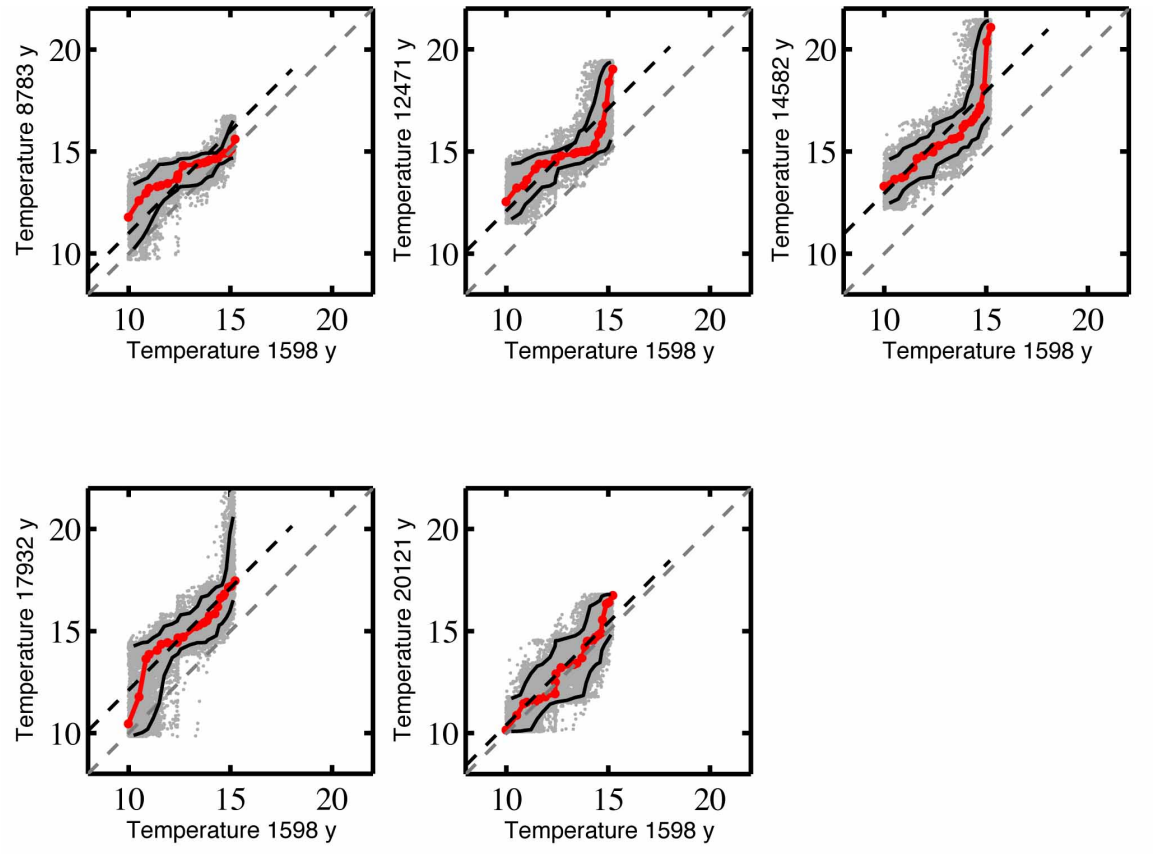

Fig. S15

Q-Q plots of Sadekov et al. (2013) Mg/Ca-derived temperatures of individual *N. dutertrei* from the Late Holocene core top in comparison to LGM interval. Resampling of pdf distribution (red line), Monte Carlo simulation (grey dots) and mean adjusted one-to-one line (black line).

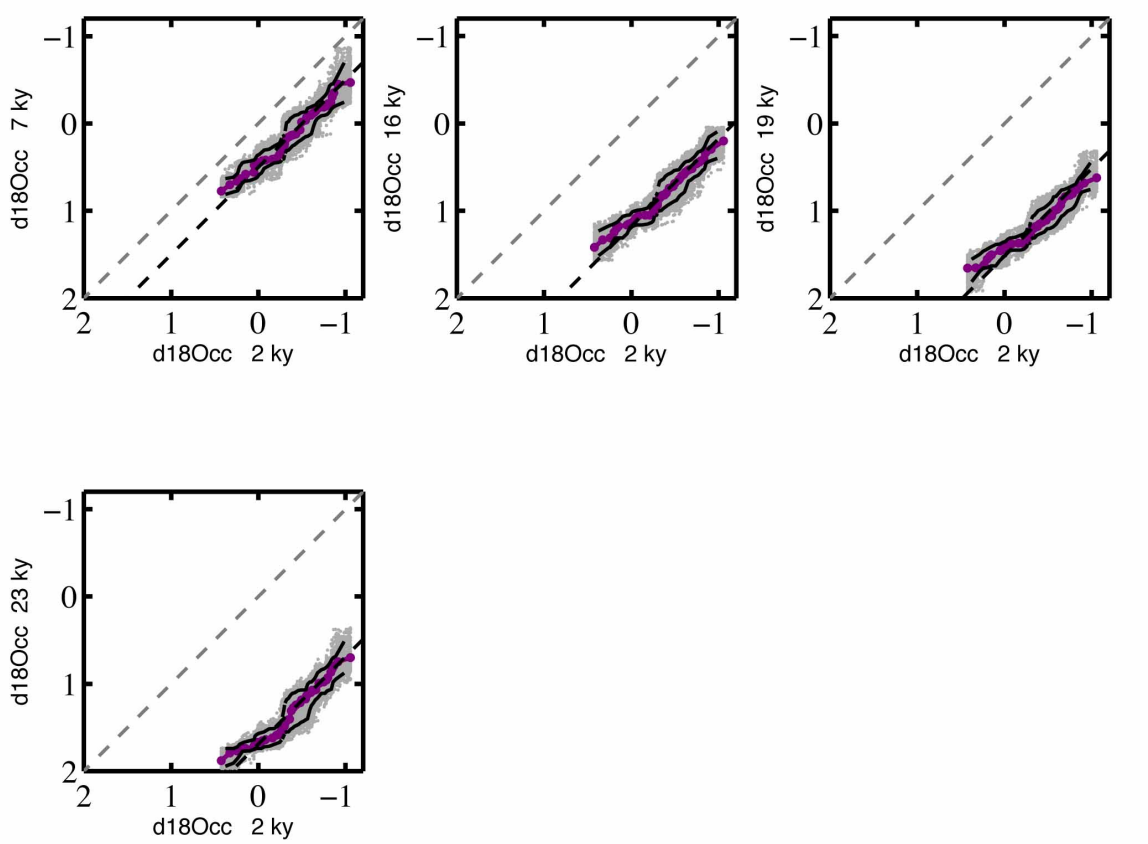

Fig. S16

Q-Q plots of Leduc et al. (2009) $\delta^{18}O$ values of individual *N. dutertrei* from the Late Holocene core top in comparison to LGM interval. Resampling of pdf distribution (purple line), Monte Carlo simulation (grey dots) and mean adjusted one-to-one line (black line).

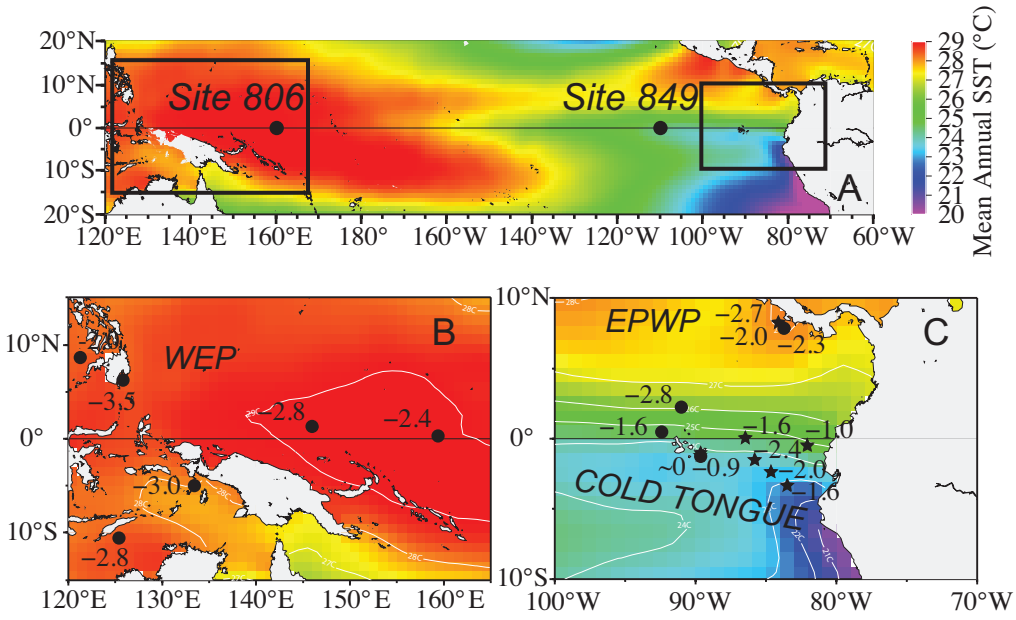

Fig. S17

SST map of the Equatorial Pacific. Mean annual sea surface temperature map using the Met Office Hadley Centre's HadISST 1.1 data set (A, Rayner et al., 2003). Inset maps of WEP (B) and EEP (C) show SST anomalies calculated from published LGM (18-20 ka) SST values minus published Holocene (4-6 ka) values at each site. Larger anomalies in the WEP compared to the EEP indicate a reduction in zonal equatorial SST gradient. Locations using Mg/Ca proxy are denoted in circles while locations using the alkenone proxy are denoted with stars.

Table S1.
Sample information and ages

Leg	Site	H	Core	Type	Section	Top (cm)	Bottom (cm)	Depth (mbsf)	Depth (mcd)	Age (cal. Y BP)
130	806	A	1	H	1	0	2	0	0	3000
130	806	A	1	H	1	51	53	0.51	0.53	19000
130	806	A	1	H	1	53	55	0.53	0.55	20000
138	849	A	1	H	1	6	8	0.06	0.06	2800
138	849	B	1	H	1	15	18	0.15	0.15	5600
138	849	B	1	H	1	74	80	0.74	0.74	20300
138	849	B	1	H	1	85	87	0.85	0.85	21500

Table S2.
Site information and depth intervals

ODP Site	*Lat*	*Long*	*Depth (m)*	*mid-Holocene*	*Last Glacial Maximum*	*Glacial Period*
806	0	159°E	2520	806A 1H-1 0-2 cm	806A 1H-1 51-53 cm 806A 1H-1 53-55 cm*	
849	0	110°W	3839	849A 1H-1 6-8 cm 849B 1H-1 15-18 cm	849B 1H-1 74-80 cm	849B 1H-1 85-87 cm

*Intervals combined for *G. tumida* only

Table S3.

Previously generated SST records used to compare mean annual and WEP-EEP gradient reconstructions to our generated SST variability.

Reference	Region	Method	Site	Lat	Long	Depth (m)	Holocene (4-6 ka) Mean	LGM (18-20 ka) Mean
Kienast et al, 2001	EEP	Uk37	ME0005A-24JC	Eq	93.5 W	2941	24.4	22.8
Koutavas & Sachs, 2008	EEP	Uk37	RC11-238	1.5 S	94.2 W	2573	24.3	21.9
Koutavas & Sachs, 2008	EEP	Uk37	V19-27	0.5 S	97.9 W	1373	25.4	24.4
Koutavas & Sachs, 2008	EEP	Uk37	V19-28	2.4 S	95.4 W	2720	23.5	21.5
Koutavas & Sachs, 2008	EEP	Uk37	V19-30	3.4 S	96.5 W	3091	22.3	20.7
Koutavas & Sachs, 2008	EEP	Uk37	V21-30	1.2 S	90.3 W	617	24.6	23.7
Lea et al., 2000	EEP	Mg/Ca	TR163-19	2.3 N	89.0 W	2348	25.9	23.1
Lea et al., 2006	EEP	Mg/Ca	TR163-22	0.5 N	87.6 W	2830	24.2	22.6
Koutavas et al., 2002	EEP	Mg/Ca	V21-30	1.2 S	90.3 W	617	22.0	21.9
Leduc et al., 2007	EPWP	Uk37	MD02-2529	8.2 N	95.9 W	1619	27.9	25.6
Benway et al., 2006	EPWP	Mg/Ca	ME0005A-43JC	7.9 N	96.4 W	1368	26.3	23.7
Benway et al., 2006	EPWP	Mg/Ca	ODP-1242	7.9 N	96.4 W	1364	26.2	24.3
de Garidel-Thoron et al, 2007	WEP	Mg/Ca	MD97-2138	1.3 N	146.1 E	1960	29.4	26.6
Rosenthal et al, 2003	WEP	Mg/Ca	MD97-2141	8.8 N	121.3 E	3600	28.8	26.8
Stott et al., 2007	WEP	Mg/Ca	MD98-2170	10.6 S	125.4 E	832	29.2	26.3
Stott et al., 2007	WEP	Mg/Ca	MD98-2176	5.0 S	133.4 E	2382	29.2	26.2
Stott et al., 2007	WEP	Mg/Ca	MD98-2181	6.3 N	125.8 E	2114	29.4	25.9
Lea et al., 2000	WEP	Mg/Ca	ODP-806B	0.3 N	159.4 E	2520	28.7	26.3

Additional Database Table S1.
Individual *G. sacculifer* and *G. tumida* temperature values at ODP Sites 806 and 849.

References and Notes

1. W. Wang, M. J. McPhaden, The surface-layer heat balance in the equatorial Pacific Ocean. Part I: Mean seasonal cycle. *J. Phys. Oceanogr.* **29**, 1812–1831 (1999). doi:10.1175/1520-0485(1999)029<1812:TSLHBI>2.0.CO;2

2. W. Wang, M. J. McPhaden, The surface-layer heat balance in the equatorial Pacific Ocean. Part II: Interannual variability. *J. Phys. Oceanogr.* **30**, 2989–3008 (2000). doi:10.1175/1520-0485(2001)031<2989:TSLHBI>2.0.CO;2

3. A. V. Fedorov, S. Philander, A stability analysis of tropical ocean-atmosphere interactions: Bridging measurements and theory for El Nino. *J. Clim.* **14**, 3086–3101 (2001). doi:10.1175/1520-0442(2001)014<3086:ASAOTO>2.0.CO;2

4. F.-F. Jin, S. T. Kim, L. Bejarano, A coupled-stability index for ENSO. *Geophys. Res. Lett.* **33**, L23708 (2006). doi:10.1029/2006GL027221

5. E. Guilyardi, A. Wittenberg, A. Fedorov, M. Collins, C. Wang, A. Capotondi, G. J. van Oldenborgh, T. Stockdale, Understanding El Niño in ocean–atmosphere general circulation models: Progress and challenges. *Bull. Am. Meteorol. Soc.* **90**, 325–340 (2009). doi:10.1175/2008BAMS2387.1

6. S.-I. An, F.-F. Jin, Collective role of thermocline and zonal advective feedbacks in the ENSO mode. *J. Clim.* **14**, 3421–3432 (2001). doi:10.1175/1520-0442(2001)014<3421:CROTAZ>2.0.CO;2

7. J. Choi, S.-I. An, S.-W. Yeh, Decadal amplitude modulation of two types of ENSO and its relationship with the mean state. *Clim. Dyn.* **38**, 2631–2644 (2012). doi:10.1007/s00382-011-1186-y

8. G. A. Schmidt, J. D. Annan, P. J. Bartlein, B. I. Cook, E. Guilyardi, J. C. Hargreaves, S. P. Harrison, M. Kageyama, A. N. LeGrande, B. Konecky, S. Lovejoy, M. E. Mann, V. Masson-Delmotte, C. Risi, D. Thompson, A. Timmermann, L.-B. Tremblay, P. Yiou, Using palaeo-climate comparisons to constrain future projections in CMIP5. *Clim. Past* **10**, 221–250 (2014). doi:10.5194/cp-10-221-2014

9. B. L. Otto-Bliesner, R. Schneider, E. C. Brady, M. Kucera, A. Abe-Ouchi, E. Bard, P. Braconnot, M. Crucifix, C. D. Hewitt, M. Kageyama, O. Marti, A. Paul, A. Rosell-Melé, C. Waelbroeck, S. L. Weber, M. Weinelt, Y. Yu, A comparison of PMIP2 model simulations and the MARGO proxy reconstruction for tropical sea surface temperatures at last glacial maximum. *Clim. Dyn.* **32**, 799–815 (2009). doi:10.1007/s00382-008-0509-0

10. J. C. Wit, G.-J. Reichart, S. J. A. Jung, D. Kroon, Approaches to unravel seasonality in sea surface temperatures using paired single-specimen foraminiferal $\delta^{18}O$ and Mg/Ca analyses. *Paleoceanography* **115**, PA4220 (2010). doi:10.1029/2009PA001857

11. A. Koutavas, S. Joanides, El Niño–Southern Oscillation extrema in the Holocene and Last Glacial Maximum. *Paleoceanography* **27**, PA4208 (2012). doi:10.1029/2012PA002378

12. A. Y. Sadekov, R. Ganeshram, L. Pichevin, R. Berdin, E. McClymont, H. Elderfield, A. W. Tudhope, Palaeoclimate reconstructions reveal a strong link between El Niño-Southern

Oscillation and Tropical Pacific mean state. *Nat. Commun.* **4**, 2692 (2013). Medline doi:10.1038/ncomms3692

13. G. Leduc, L. Vidal, O. Cartapanis, E. Bard, Modes of eastern equatorial Pacific thermocline variability: Implications for ENSO dynamics over the last glacial period. *Paleoceanography* **24**, PA3202 (2009). doi:10.1029/2008PA001701

14. S.-I. An, F.-F. Jin, Nonlinearity and asymmetry of ENSO. *J. Clim.* **17**, 2399–2412 (2004). doi:10.1175/1520-0442(2004)017<2399:NAAOE>2.0.CO;2

15. J. Boucharel, B. Dewitte, Y. du Penhoat, B. Garel, S.-W. Yeh, J.-S. Kug, ENSO nonlinearity in a warming climate. *Clim. Dyn.* **37**, 2045–2065 (2011). doi:10.1007/s00382-011-1119-9

16. D. W. Lea, The 100 000-yr cycle in tropical SST, greenhouse forcing, and climate sensitivity. *J. Clim.* **17**, 2170–2179 (2004). doi:10.1175/1520-0442(2004)017<2170:TYCITS>2.0.CO;2

17. T. Sagawa, Y. Yokoyama, M. Ikehara, M. Kuwae, Vertical thermal structure history in the western subtropical North Pacific since the Last Glacial Maximum. *Geophys. Res. Lett.* **38**, L00F02 (2011). doi:10.1029/2010GL045827

18. P. N. DiNezio, A. Clement, G. A. Vecchi, B. Soden, A. J. Broccoli, B. L. Otto-Bliesner, P. Braconnot, The response of the Walker circulation to Last Glacial Maximum forcing: Implications for detection in proxies. *Paleoceanography* **26**, PA3217 (2011). doi:10.1029/2010PA002083

19. D. H. Andreasen, A. C. Ravelo, Tropical Pacific Ocean thermocline depth reconstructions for the last glacial maximum. *Paleoceanography* **12**, 395–413 (1997). doi:10.1029/97PA00822

20. J. Xu, W. Kuhnt, A. Holbourn, M. Regenberg, N. Andersen, Indo-Pacific Warm Pool variability during the Holocene and Last Glacial Maximum. *Paleoceanography* **25**, PA4230 (2010). doi:10.1029/2010PA001934

21. P. Fiedler, L. Talley, Hydrography of the eastern tropical Pacific: A review. *Prog. Oceanogr.* **69**, 143–180 (2006). doi:10.1016/j.pocean.2006.03.008

22. K. Thirumalai, J. W. Partin, C. S. Jackson, T. M. Quinn, Statistical constraints on El Niño Southern Oscillation reconstructions using individual foraminifera: A sensitivity analysis. *Paleoceanography* **28**, 401–412 (2013). doi:10.1002/palo.20037

23. E. C. Brady, B. L. Otto-Bliesner, J. E. Kay, N. Rosenbloom, Sensitivity to glacial forcing in the CCSM4. *J. Clim.* **26**, 1901–1925 (2013). doi:10.1175/JCLI-D-11-00416.1

24. A. Patrick, R. Thunell, Tropical Pacific sea surface temperatures and upper water column thermal structure during the last glacial maximum. *Paleoceanography* **12**, 649–657 (1997). doi:10.1029/97PA01553

25. H. Spero, K. Mielke, E. Kalve, D. Lea, D. Pak, Multispecies approach to reconstructing eastern equatorial Pacific thermocline hydrography during the past 360 kyr. *Paleoceanography* **18**, 1022 (2003). doi:10.1029/2002PA000814

26. D. Rincón-Martínez, S. Steph, F. Lamy, A. Mix, R. Tiedemann, Tracking the equatorial front in the eastern equatorial Pacific Ocean by the isotopic and faunal composition of

planktonic foraminifera. *Mar. Micropaleontol.* **79**, 24–40 (2011). doi:10.1016/j.marmicro.2011.01.001

27. H. M. Benway, A. C. Mix, B. A. Haley, G. P. Klinkhammer, Eastern Pacific Warm Pool paleosalinity and climate variability: 0–30 kyr. *Paleoceanography* **21**, PA3008 (2006). doi:10.1029/2005PA001208

28. A. Koutavas, J. Lynch-Stieglitz, T. M. Marchitto Jr., J. P. Sachs, El Niño-like pattern in ice age tropical Pacific sea surface temperature. *Science* **297**, 226–230 (2002). Medline doi:10.1126/science.1072376

29. G. E. Manucharyan, A. V. Fedorov, Robust ENSO across a wide range of climates. *J. Clim.* **27**, 5836–5850 (2014). doi:10.1175/JCLI-D-13-00759.1

30. Z.-Z. Hu, A. Kumar, H.-L. Ren, H. Wang, M. L'Heureux, F.-F. Jin, Weakened interannual variability in the tropical Pacific Ocean since 2000. *J. Clim.* **26**, 2601–2613 (2013). doi:10.1175/JCLI-D-12-00265.1

31. M. Collins, S.-I. An, W. Cai, A. Ganachaud, E. Guilyardi, F.-F. Jin, M. Jochum, M. Lengaigne, S. Power, A. Timmermann, G. Vecchi, A. Wittenberg, The impact of global warming on the tropical Pacific Ocean and El Niño. *Nat. Geosci.* **3**, 391–397 (2010). doi:10.1038/ngeo868

32. N. A. Rayner, D. E. Parker, E. B. Horton, C. K. Folland, L. V. Alexander, D. P. Rowell, E. C. Kent, A. Kaplan, Global analyses of sea surface temperature, sea ice, and night marine air temperature since the late nineteenth century. *J. Geophys. Res.* **108**, 4407 (2003). doi:10.1029/2002JD002670

33. A. W. Tudhope, C. P. Chilcott, M. T. McCulloch, E. R. Cook, J. Chappell, R. M. Ellam, D. W. Lea, J. M. Lough, G. B. Shimmield, Variability in the El Niño-Southern Oscillation through a glacial-interglacial cycle. *Science* **291**, 1511–1517 (2001). Medline doi:10.1126/science.1057969

34. B. Rein, A. Lückge, L. Reinhardt, F. Sirocko, A. Wolf, W.-C. Dullo, El Niño variability off Peru during the last 20,000 years. *Paleoceanography* **20**, PA4003 (2005). doi:10.1029/2004PA001099

35. T. Bickert, W. H. Berger, S. Burke, H. Schmidt, G. Wefer, Late Quaternary stable isotope record of benthic foraminifers: Sites 805 and 806, Ontong Java Plateau. in *Proc. ODP, Sci. Results*, W. Berger *et al*., Eds. (Ocean Drilling Program, College Station, TX, 1993), vol. 130, pp. 411–420; doi:10.2973/odp.proc.sr.130.025.1993.

36. A. C. Mix, N. G. Pisias, W. Rugh, J. Wilson, A. Morey, T. K. Hagelberg, Benthic foraminifer stable isotope recond from Site 849 (0–5 Ma): Local and global climate changes. in *Proc. ODP, Sci. Results*, N. G. Pisias L. A. Mayer, T. R. Janecek, A. Palmer-Julson, T. H. van Andel, Eds. (Ocean Drilling Program, College Station, TX, 1995), vol. 138, pp. 371–412; doi:10.2973/odp.proc.sr.138.120.1995.

37. D. Paillard, L. Labeyrie, P. Yiou, Macintosh program performs time-series analysis. *Eos Trans. AGU* **77**, 379 (1996). doi:10.1029/96EO00259

38. B. K. Linsley, Oxygen-isotope record of sea level and climate variations in the Sulu Sea over the past 150,000 years. *Nature* **380**, 234–237 (1996). doi:10.1038/380234a0

39. A. Koutavas, J. P. Sachs, Northern timing of deglaciation in the eastern equatorial Pacific from alkenone paleothermometry. *Paleoceanography* **23**, PA4205 (2008). doi:10.1029/2008PA001593

40. A. C. Ravelo, R. G. Fairbanks, Oxygen isotopic composition of multiple species of planktonic foraminifera: Recorders of the modern photic zone temperature gradient. *Paleoceanography* **7**, 815–831 (1992). doi:10.1029/92PA02092

41. S. Eggins, P. Dedeckker, J. Marshall, Mg/Ca variation in planktonic foraminifera tests: Implications for reconstructing palaeo-seawater temperature and habitat migration. *Earth Planet. Sci. Lett.* **212**, 291–306 (2003). doi:10.1016/S0012-821X(03)00283-8

42. A. Sadekov, S. M. Eggins, P. De Deckker, D. Kroon, Uncertainties in seawater thermometry deriving from intratest and intertest Mg/Ca variability in *Globigerinoides ruber*. *Paleoceanography* **23**, PA1215 (2008). doi:10.1029/2007PA001452

43. L. Vetter, R. Kozdon, C. I. Mora, S. M. Eggins, J. W. Valley, B. Hönisch, H. J. Spero, Micron-scale intrashell oxygen isotope variation in cultured planktic foraminifers. *Geochim. Cosmochim. Acta* **107**, 267–278 (2013). doi:10.1016/j.gca.2012.12.046

44. M. Regenberg, D. Nürnberg, S. Steph, J. Groeneveld, D. Garbe-Schönberg, R. Tiedemann, W.-C. Dullo, Assessing the effect of dissolution on planktonic foraminiferal Mg/Ca ratios: Evidence from Caribbean core tops. *Geochem. Geophys. Geosyst.* **7**, Q07P15 (2006). doi:10.1029/2005GC001019

45. P. Anand, H. Elderfield, M. Conte, Calibration of Mg/Ca thermometry in planktonic foraminifera from a sediment trap time series. *Paleoceanography* **18**, 1050 (2003). doi:10.1029/2002PA000846

46. R. M. Key, A. Kozyr, C. L. Sabine, K. Lee, R. Wanninkhof, J. L. Bullister, R. A. Feely, F. J. Millero, C. Mordy, T.-H. Peng, A global ocean carbon climatology: Results from Global Data Analysis Project (GLODAP). *Global Biogeochem. Cycles* **18**, GB4031 (2004). doi:10.1029/2004GB002247

47. A. R. Locarnini *et al.*, *World Ocean Atlas 2009*, S. Levitus, Ed. (U.S. Government Printing Office, Washington, DC, 2010).

48. J. Yu, W. S. Broecker, H. Elderfield, Z. Jin, J. McManus, F. Zhang, Loss of carbon from the deep sea since the Last Glacial Maximum. *Science* **330**, 1084–1087 (2010). Medline doi:10.1126/science.1193221

49. E. Boyle, L. Keigwin, Comparison of the Atlantic and Pacific paleochemical records for the last 215,000 years: Changes in deep ocean circulation and chemical inventories. *Earth Planet. Sci. Lett.* **76**, 135–150 (1985). doi:10.1016/0012-821X(85)90154-2

50. P. A. Martin, D. W. Lea, A simple evaluation of cleaning procedures on fossil benthic foraminiferal Mg/Ca. *Geochem. Geophys. Geosyst.* **3**, 8401 (2002). doi:10.1029/2001GC000280

51. M. W. Wara, L. D. Anderson, S. A. Schellenberg, R. Franks, A. C. Ravelo, M. L. Delaney, Application of a radially viewed inductively coupled plasma-optical emission spectrophotometer to simultaneous measurement of Mg/Ca, Sr/Ca, and Mn/Ca ratios in

marine biogenic carbonates. *Geochem. Geophys. Geosyst.* **4**, 8406 (2003). doi:10.1029/2003GC000525

52. M. Mohtadi, D. W. Oppo, A. Lückge, R. DePol-Holz, S. Steinke, J. Groeneveld, N. Hemme, D. Hebbeln, Reconstructing the thermal structure of the upper ocean: Insights from planktic foraminifera shell chemistry and alkenones in modern sediments of the tropical eastern Indian Ocean. *Paleoceanography* **26**, PA3219 (2011). doi:10.1029/2011PA002132

53. J. A. Carton, B. S. Giese, A reanalysis of ocean climate using Simple Ocean Data Assimilation (SODA). *Mon. Weather Rev.* **136**, 2999–3017 (2008). doi:10.1175/2007MWR1978.1

54. H. Kawahata, A. Nishimura, M. K. Gagan, Seasonal change in foraminiferal production in the western equatorial Pacific warm pool: Evidence from sediment trap experiments. *Deep-Sea Res. Part II* **49**, 2783–2800 (2002). doi:10.1016/S0967-0645(02)00058-9

55. R. Thunell, L. A. Reynolds, Sedimentation of planktonic foraminifera: Seasonal-Changes in species flux in the Panama Basin. *Micropaleontology* **30**, 243–262 (1984). doi:10.2307/1485688

56. P. S. Dekens, D. W. Lea, D. K. Pak, H. J. Spero, Core top calibration of Mg/Ca in tropical foraminifera: Refining paleotemperature estimation. *Geochem. Geophys. Geosyst.* **3**, 1–29 (2002). doi:10.1029/2001GC000200

57. B. Wang, R. Wu, R. Lukas, Annual adjustment of the thermocline in the tropical Pacific Ocean. *J. Clim.* **13**, 596–616 (2000). doi:10.1175/1520-0442(2000)013<0596:AAOTTI>2.0.CO;2

58. L. D. Stott, C. M. Tang, Reassessment of foraminiferal-based tropical sea surface $\delta^{18}O$ paleotemperatures. *Paleoceanography* **11**, 37–56 (1996). doi:10.1029/95PA03344

59. A. N. LeGrande, G. A. Schmidt, Global gridded data set of the oxygen isotopic composition in seawater. *Geophys. Res. Lett.* **33**, L12604 (2006). doi:10.1029/2006GL026011

60. B. Bemis, H. Spero, J. Bijma, D. Lea, Reevaluation of the oxygen isotopic composition of planktonic foraminifera: Experimental results and revised paleotemperature equations. *Paleoceanography* **13**, 150–160 (1998). doi:10.1029/98PA00070

61. A. Timmermann, S. J. Lorenz, S.-I. An, A. Clement, S.-P. Xie, The effect of orbital forcing on the mean climate and variability of the tropical Pacific. *J. Clim.* **20**, 4147–4159 (2007). doi:10.1175/JCLI4240.1

62. K. Faul, A. C. Ravelo, M. Delaney, Reconstructions of upwelling productivity, and photic zone depth in the eastern equatorial Pacific Ocean using planktonic foraminiferal stable isotopes and abunances. *J. Foraminiferal Res.* **30**, 110–125 (2000). doi:10.2113/0300110

63. C. Wang, P. Fiedler, ENSO variability and the eastern tropical Pacific: A review. *Prog. Oceanogr.* **69**, 239–266 (2006). doi:10.1016/j.pocean.2006.03.004

64. D. W. Lea, D. K. Pak, H. J. Spero, Climate impact of late quaternary equatorial pacific sea surface temperature variations. *Science* **289**, 1719–1724 (2000). Medline doi:10.1126/science.289.5485.1719

65. Y. Rosenthal, D. Oppo, B. K. Linsley, The amplitude and phasing of climate change during the last deglaciation in the Sulu Sea, western equatorial Pacific. *Geophys. Res. Lett.* **30**, 1428 (2003). doi:10.1029/2002GL016612

66. M. Kienast, S. S. Kienast, S. E. Calvert, T. I. Eglinton, G. Mollenhauer, R. François, A. C. Mix, Eastern Pacific cooling and Atlantic overturning circulation during the last deglaciation. *Nature* **443**, 846–849 (2006). Medline doi:10.1038/nature05222

67. D. W. Lea, D. K. Pak, C. L. Belanger, H. J. Spero, M. A. Hall, N. J. Shackleton, Paleoclimate history of Galapagos surface waters over the last 135,000 yr. *Quat. Sci. Rev.* **25**, 1152–1167 (2006). doi:10.1016/j.quascirev.2005.11.010

68. T. de Garidel-Thoron, Y. Rosenthal, L. Beaufort, E. Bard, C. Sonzogni, A. C. Mix, A multiproxy assessment of the western equatorial Pacific hydrography during the last 30 kyr. *Paleoceanography* **22**, PA3204 (2007). doi:10.1029/2006PA001269

69. G. Leduc, L. Vidal, K. Tachikawa, F. Rostek, C. Sonzogni, L. Beaufort, E. Bard, Moisture transport across Central America as a positive feedback on abrupt climatic changes. *Nature* **445**, 908–911 (2007). Medline doi:10.1038/nature05578

70. L. Stott, A. Timmermann, R. Thunell, Southern Hemisphere and deep-sea warming led deglacial atmospheric CO_2 rise and tropical warming. *Science* **318**, 435–438 (2007). Medline doi:10.1126/science.1143791